

X-ray source population study of the starburst galaxy M 83 with *XMM-Newton*^{★,★★,★★★}

L. Ducci¹, M. Sasaki¹, F. Haberl², and W. Pietsch²

¹ Institut für Astronomie und Astrophysik, Eberhard Karls Universität, Sand 1, 72076 Tübingen, Germany
 e-mail: ducci@astro.uni-tuebingen.de

² Max-Planck-Institut für Extraterrestrische Physik, Giessenbachstraße, 85741 Garching, Germany

Received 3 January 2013 / Accepted 5 March 2013

ABSTRACT

Aims. We present the results obtained from the analysis of three *XMM-Newton* observations of M 83. The aims of the paper are studying the X-ray source populations in M 83 and calculating the X-ray luminosity functions of X-ray binaries for different regions of the galaxy.

Methods. We detected 189 sources in the *XMM-Newton* field of view in the energy range of 0.2–12 keV. We constrained their nature by means of spectral analysis, hardness ratios, studies of the X-ray variability, and cross-correlations with catalogues in X-ray, optical, infrared, and radio wavelengths.

Results. We identified and classified 12 background objects, five foreground stars, two X-ray binaries, one supernova remnant candidate, one super-soft source candidate and one ultra-luminous X-ray source. Among these sources, we classified for the first time three active galactic nuclei (AGN) candidates. We derived X-ray luminosity functions of the X-ray sources in M 83 in the 2–10 keV energy range, within and outside the D_{25} ellipse, correcting the total X-ray luminosity function for incompleteness and subtracting the AGN contribution. The X-ray luminosity function inside the D_{25} ellipse is consistent with that previously observed by *Chandra*. The Kolmogorov-Smirnov test shows that the X-ray luminosity function of the outer disc and the AGN luminosity distribution are uncorrelated with a probability of $\sim 99.3\%$. We also found that the X-ray sources detected outside the D_{25} ellipse and the uniform spatial distribution of AGNs are spatially uncorrelated with a significance of 99.5%. We interpret these results as an indication that part of the observed X-ray sources are X-ray binaries in the outer disc of M 83.

Key words. galaxies: individual: M 33 – X-rays: galaxies

1. Introduction

M 83 (NGC 5236) is a grand-design barred spiral galaxy (SAB(s)c; de Vaucouleurs et al. 1992) located at 4.5 ± 0.3 Mpc from the Milky Way (Thim et al. 2003). M 83 is oriented nearly face-on ($i = 24^\circ$; Rogstad et al. 1974) and shows a galactic disc spanning $12.9' \times 11.5'$ ($17 \text{ kpc} \times 15.2 \text{ kpc}$; Wofford et al. 2011).

M 83 is experiencing a starburst activity with a present-day star formation rate (SFR) of $3\text{--}4 M_\odot \text{ yr}^{-1}$ (Boissier et al. 2005) in three regions: the nuclear region (galactocentric distance $d \lesssim 300 \text{ pc}$; Harris et al. 2001), the inner disc ($300 \text{ pc} \lesssim d \lesssim 7.5 \text{ kpc}$), and the outer disc ($7.5 \text{ kpc} \lesssim d \lesssim 20 \text{ kpc}$; Dong et al. 2008). Ultraviolet (UV) images of M 83 obtained with the Galaxy Evolution Explorer (GALEX) satellite revealed a population of young stars ($\lesssim 400 \text{ Myr}$) in the outer disc of M 83 (Thilker et al. 2005). Although this would indicate recent star-forming activity, using *Spitzer* and GALEX data, Dong et al. (2008) discovered that the star formation in the outer disc started at least 1 Gyr ago. These results are confirmed by the study of AGB stars of Davidge (2010). Bigiel et al. (2010) compared the HI data from

the National Radio Astronomy Observatory (NRAO) Very Large Array (VLA) and far-ultraviolet (FUV) data from GALEX in the outer disc of M 83, and discovered that the star formation traced by the FUV emission and HI are spatially correlated out to almost four optical radii. Bigiel et al. (2010) also found that the star formation rate in the outer disc ($\sim 0.01 M_\odot \text{ yr}^{-1}$; Bresolin et al. 2009) implies that the star formation activity is not completely consuming the HI reservoir, which will be available as fuel for star formation in the inner disc.

M 83 was observed in the X-ray bands by *Einstein* in 1979–1981 (Trinchieri et al. 1985), Ginga in 1987 (Ohashi et al. 1990), ROSAT in 1992–1994 (Ehle et al. 1998; Immler et al. 1999), ASCA in 1994 (Okada et al. 1997), and *Chandra* in 2000 (Soria & Wu 2002; Soria & Wu 2003, SW03 hereafter). SW03 identified 127 discrete sources near the centre of M 83 ($8.3' \times 8.3'$) and resolved for the first time the nuclear region in X-rays. The diffuse X-ray emission of M 83 has been studied by Owen & Warwick (2009) with an *XMM-Newton* observation performed in January 27, 2003 (obsid 0110910201). They obtained a good fit to the spectrum assuming a two-temperature thermal model, which is typical of the diffuse emission in normal and starburst galaxies. They also found that the soft X-ray emission mainly overlaps with the inner spiral arm, and shows a strong correlation with the distribution of UV emission, indicative of a correlation between X-ray emission and recent star formation.

The recent high star formation activity experienced by the nucleus and the spiral arms of M 83 provided an unusually large number of supernova remnants (SNRs). In

* Based on observations obtained with *XMM-Newton*, an ESA science mission with instruments and contributions directly funded by ESA Member States and NASA.

** Appendix A is available in electronic form at <http://www.aanda.org>

*** Appendix B is only available at the CDS via anonymous ftp to [cdsarc.u-strasbg.fr](ftp://cdsarc.u-strasbg.fr) (130.79.128.5) or via <http://cdsarc.u-strasbg.fr/viz-bin/qcat?J/A+A/553/A7>

Table 1. *XMM-Newton* observations of M 83.

	Obs. ID.	Date	Pointing direction		EPIC PN		EPIC MOS1		EPIC MOS2		Mode	
			RA	Dec	filter	T_{exp}	filter	T_{exp}	filter	T_{exp}	PN	MOS
1	0110910201	2003-01-27	13:37:05.16	-29:51:46.1	thin	21.2	medium	24.6	medium	24.6	EFF	FF
2	0503230101	2008-01-16	13:37:01.09	-30:03:49.9	medium	15.4	medium	19.0	medium	19.0	EFF	FF
3	0552080101	2008-08-16	13:36:50.87	-30:03:55.2	medium	25.0	medium	28.8	medium	28.8	EFF	FF

Notes. The exposure times after the screening for high background are given in units of ks. Mode: EFF = extended full frame imaging mode; FF = full frame imaging mode.

fact, the optical survey performed at the Cerro Tololo Inter-American Observatory in Chile by Blair & Long (2004) identified 71 sources as SNR candidates, the *Hubble* Space Telescope (HST) observations of the nuclear region of M 83 (Dopita et al. 2010) provided the identification of 60 SNR candidates, and the Magellan I survey 271 SNR candidates (Blair et al. 2012).

In a normal galaxy such as M 83, X-ray binaries (XRBs) are the most prominent class of X-ray sources. XRBs show X-ray luminosities ranging from $\sim 10^{32}$ erg s $^{-1}$ to the Eddington luminosity, and sometimes they can exceed this limit (see e.g. White & Carpenter 1978). They are composed of a compact object (a neutron star or a black hole) and a companion star, which can be a main-sequence, giant, or supergiant star, and in some cases a white dwarf (e.g. van Paradijs 1998). The strong X-ray emission is produced by the accretion of matter from the companion star onto the compact object. XRBs are usually divided into two classes: low mass X-ray binaries (LMXBs), and high mass X-ray binaries (HMXBs). The companion stars of LMXBs have masses lower than $\sim 1 M_{\odot}$. The lifetime of an LMXB is determined by the nuclear evolution time-scale of the companion star to 10^8 – 10^9 yr (e.g. Tauris & van den Heuvel 2006), and their number is correlated to the total stellar mass of a galaxy (Gilfanov 2004). The companion star of LMXBs usually transfers mass by Roche-lobe overflow, and the compact object accretes from an accretion disc (e.g. van Paradijs 1998). The donors in HMXBs have masses $\geq 8 M_{\odot}$, and their typical lifetime does not exceed 10^6 – 10^7 yr. Therefore, the presence of HMXBs in a particular region of a galaxy is associated with a relatively recent star formation event (e.g. Fabbiano 2006). The X-ray emission from HMXBs is usually explained with the accretion of a fraction of the stellar wind ejected by the donor star onto the compact object, or through mass transfer via Roche-lobe overflow (see e.g. Treves et al. 1988 and references therein). As a first approximation, two standard models are commonly used to describe the X-ray spectra of XRBs in nearby galaxies: an absorbed disc-blackbody model, with temperatures ranging from ~ 0.5 to ~ 1 keV (e.g. Makishima et al. 1986), or an absorbed powerlaw model. X-ray spectra of LMXBs below 10 keV are described by absorbed powerlaw with photon indices 1–3. HMXBs usually show harder X-ray spectra in the energy range 1–10 keV, with photon indices 1–2 and a high intrinsic absorption (White et al. 1995). Within each of these classes, the properties of the X-ray spectra can also depend on the type of the accreting compact object. Accreting black holes can show states of high luminosity (e.g. Jones 1977), with very soft spectra, with slopes steeper than those shown by accreting neutron stars (see e.g. White & Marshall 1984). Given the wide variety of spectral shapes shown by XRBs, they can be confused with background AGNs, whose X-ray spectra have roughly a powerlaw shape, with indices ranging from 1.6 to 2.5 (see e.g. Walter & Fink 1993; Vignali et al. 1999; Turner et al. 1991).

In this paper we report the results obtained from a study of the X-ray source populations of M 83, using three *XMM-Newton*

observations covering both the inner and outer disc regions. The higher spatial resolution and sensitivity of *XMM-Newton* compared to the previous observations of ROSAT and *Einstein* allowed an increase of the number of detected sources in M 83. While the spatial coverage of the *Chandra* observation was limited to a region located at the centre of M 83 with a size of $8.3' \times 8.3'$ (the ACIS S3 field of view), the *XMM-Newton* observations allowed us to obtain a complete coverage of M 83, and to study also the outer parts of the galaxy, which in total provided us with a more representative sample of X-ray sources in M 83.

The paper is organised as follows: in Sect. 2 we describe the data reduction and analysis of *XMM-Newton* observations. In Sect. 3 we show the astrometrical corrections that have been applied. In Sect. 4 we present the techniques adopted to classify the X-ray sources (X-ray variability, spectral analysis, and hardness ratios). In Sect. 5 we describe the properties and classification of the detected sources. In Sect. 6 we derive the X-ray luminosity functions (XLFs) of X-ray binaries within and outside the D_{25} ellipse, after correcting them for incompleteness and subtracting the AGN contribution, and we discuss our results. We examine in detail the properties of the sources that have been identified and classified in this work in Appendix A.

2. Reduction and data analysis

We analysed the public archival *XMM-Newton* data of M 83 (PIs: Watson, Kuntz). Table 1 lists the three observations that we analysed, one pointing at the centre of the galaxy (obs. 1) and two in the south, which covered the outer arms with a young population of stars discovered with GALEX. The data analysis was performed using the *XMM-Newton* Science Analysis System (SAS) 12.0. For each pointing we produced PN, MOS1, and MOS2 event files. We excluded times of high background due to soft proton flares as follows. For each observation and instrument, we created background lightcurves (with sources removed) in the 7–15 keV energy band. Good time intervals (GTIs) were determined by selecting count rates lower than 8 cts ks $^{-1}$ arcmin $^{-2}$ and 2.5 cts ks $^{-1}$ arcmin $^{-2}$ for PN and MOS, respectively.

For each observation, data were divided into five energy bands:

- R1: 0.2–0.5 keV;
- R2: 0.5–1 keV;
- R3: 1–2 keV;
- R4: 2–4.5 keV;
- R5: 4.5–12 keV.

For the PN data we used single-pixel events (PATTERN = 0) in the first energy band and for the other energy bands single- and double-pixel events (PATTERN ≤ 4) were selected. For the MOS data, single-pixel to quadruple-pixel events (PATTERN ≤ 12) were used for all five bands.

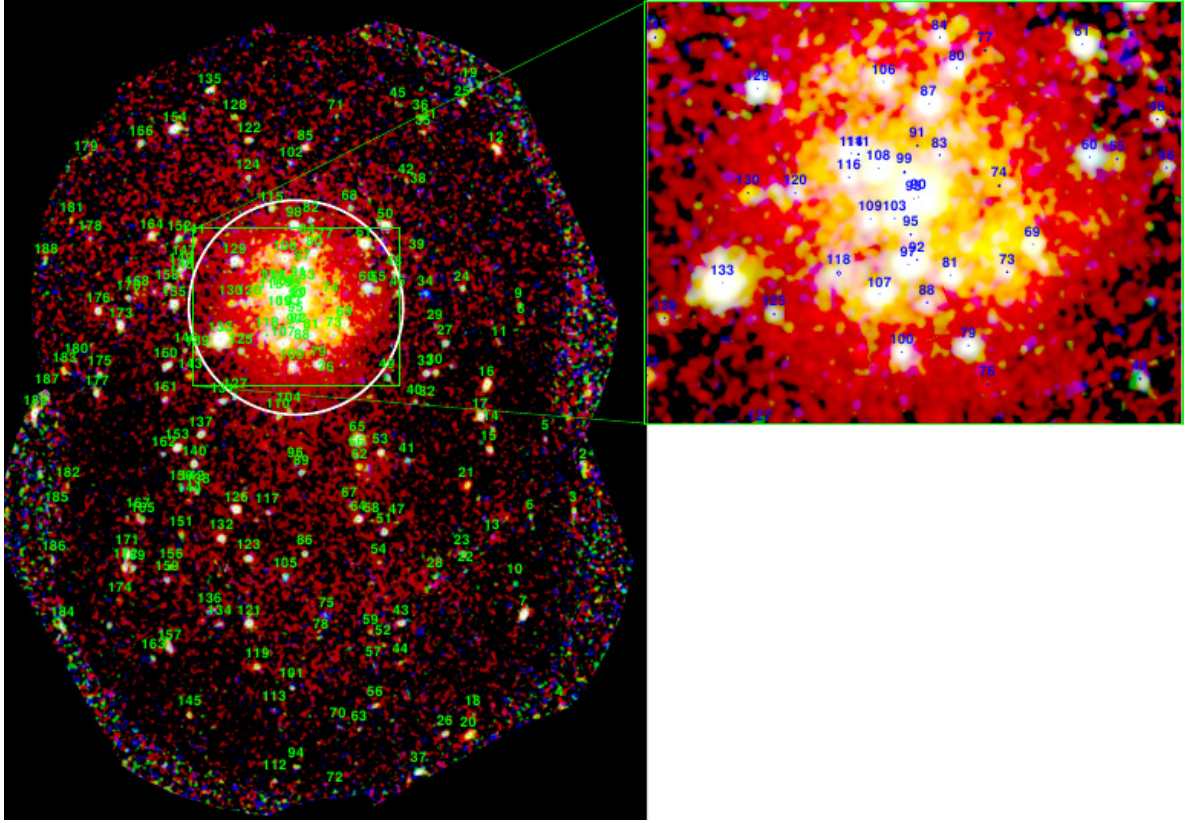


Fig. 1. Combined PN, MOS1, and MOS2 three-colour mosaic image of M 83. The crowded central region is shown in higher resolution. The white circle is the D_{25} ellipse (diameter = $11.5''$; Tully 1988).

We ran the source detection procedure separately for images of each observation, and simultaneously for five energy bands and three instruments with the SAS task `edetect_chain`. The source detection consists of three steps. The first step provides a list of source positions used to create the background maps. We adopted a minimum-detection likelihood¹ of 7 to obtain this list of sources. After removing the sources, a two-dimensional spline with 20 nodes was fitted to the exposure-corrected image. In the second step the background maps are used to improve the detection sensitivity and hence to create a new source list, assuming a minimum-detection likelihood of 4. In the last step, a maximum-likelihood point-spread function (PSF) fit to the source count distribution is performed simultaneously in all energy bands and each EPIC instrument, from the input list of source positions obtained in the previous step (a description of this algorithm is given by Cruddace et al. 1988). For each observation we generated the final source list adopting a lower threshold for the maximum-detection likelihood of 6, which corresponds to a detection probability of $\sim 99.75\%$. The source detection gives several parameters for each source, such as the coordinates, count rates, and likelihood of detection (see Table B.1). As mentioned above, 20 nodes (more than the default 16) for the background spline map were used to better follow the central diffuse emission and to minimise false detections. We removed the remaining false detections due to diffuse emission structures by visual inspection.

Figure 1 shows the combined PN, MOS1, and MOS2 three-colour mosaic image obtained from the three observations. The

numbers of the detected sources are overplotted on the image. The red, green, and blue colours represent the 0.2–1 keV, 1–2 keV, and 2–4.5 keV energy bands.

3. Astrometrical corrections

3.1. Corrections between *XMM-Newton* observations

We calculated the RA and Dec offsets of the three *XMM-Newton* observations using position of the sources detected in at least two observations. Sources were considered as detections in at least two different observations if their position was closer than $3\times$ the combined statistical positional errors. We calculated the offsets of observations 2 and 3 with respect to the reference observation 1 as the weighted mean of RA and Dec of all sources, then recalculated all X-ray positions correcting for the shifts relative to the observation 1.

3.2. Correcting the position of the detected sources using X-ray and optical observations

We also applied the cross-correlation procedure described above to determine the systematic errors in the X-ray positions of the *XMM-Newton* observations by calculating the offsets in the X-ray positions of the *XMM-Newton* sources with respect to the X-ray sources observed by SW03 with *Chandra*. The offset between the *XMM-Newton* and *Chandra* positions (given as the weighted mean of RA and Dec in arcsec) is $\Delta\text{RA} = -1.22 \pm 0.16$, $\Delta\text{Dec} = -0.72 \pm 0.16$. We point out that SW03 corrected the *Chandra* positions using only the position of the infrared nucleus of M 83 deduced from HST/WFPC2 observations. Therefore, to

¹ The detection likelihood L is defined by the relationship $L = -\ln(p)$, where p is the probability that a Poissonian fluctuation in the background is detected as a spurious source.

Table 2. Count rate to energy conversion factors for thin and medium filters of the EPIC instruments in the energy ranges R1–R5.

Detector	Filter	R1	R2	R3	R4	R5
EPIC			(10 ⁻¹²) erg cm ⁻² ct ⁻¹			
PN	Thin	0.8850	1.091	1.731	5.020	17.97
	Medium	1.055	1.110	1.730	4.977	17.47
MOS	Medium	6.796	5.582	5.189	13.71	69.63

Notes. We assumed an absorbed powerlaw with a photon index of 1.7 and the Galactic foreground absorption 3.69×10^{20} cm⁻² in the direction of M 83.

obtain more accurate positions from possible optical counterparts, we cross-correlated the *XMM-Newton* list of sources with the optical catalogue of the United States Naval Observatory USNO-B1 (Monet et al. 2003). For this calculation we were interested in associations between X-ray sources and foreground stars. As discussed in Sect. 5.1, we classified five sources as foreground star candidates. The offset between the X-ray positions and optical positions corrected for proper motion (given as the weighted mean of RA and Dec in arcsec) is $\Delta\text{RA} = -2.02 \pm 0.43$, $\Delta\text{Dec} = -0.44 \pm 0.43$. The measured offset in RA agrees with the expected precision of the *XMM-Newton* Attitude Measurement System (Guainazzi 2012). We used these systematic offsets to correct the position of all detected sources.

4. Analysis

4.1. Variability of the sources

4.1.1. Short-term variability

For each *XMM-Newton* observation, we searched for pulsations of the brightest sources (counts ≥ 200) on time scales between ~ 4 s and the time duration of each observation. After extracting the event files, we applied both a Fourier transform and a Z_{tr}^2 analysis (Bucccheri et al. 1983). No statistically significant variability from the analysed sources was detected.

4.1.2. Long-term variability

To study the long-term time variability of sources observable at least in two different observations, we calculated the average flux (or the 3σ upper limit in case of non-detection) at the source position in each observation. We considered fluxes in the 0.2–4.5 keV energy band because, as Pietsch et al. (2004) noted, the band 4.5–12 keV has a lower sensitivity and is contaminated by hard background. We calculated the fluxes with the energy conversion factors (ECFs) reported in Table 2. Then, we searched for variable sources by comparing their fluxes (or upper limits) in different observations. We measured the X-ray variability of each source by its variability factor $V_i = F_{\text{max}}/F_{\text{min}}$, where F_{max} and F_{min} are the maximum and minimum (or upper-limit) fluxes. To estimate the significance of the variability between different observations, we calculated the significance parameter $S = (F_{\text{max}} - F_{\text{min}})/\sqrt{\sigma_{\text{max}}^2 + \sigma_{\text{min}}^2}$, where σ_{max} and σ_{min} are the errors of the maximum and minimum flux (Primini et al. 1993).

We also studied the X-ray variability considering the *Chandra* observation of M 83. We converted the *Chandra* counts (0.3–8 keV) of SW03 to 0.2–4.5 keV fluxes with the conversion factor calculated by SW03 and the distance of M 83

($d = 4.5$ Mpc) assumed in this work. The conversion factor $CF = 8 \times 10^{37}/300$ erg s⁻¹ counts⁻¹ was calculated by SW03 assuming an absorbed powerlaw spectrum with $\Gamma = 1.7$, $N_{\text{H}} = 10^{21}$ cm⁻², and a distance of 3.7 Mpc. For each *Chandra* source, we obtained the flux in the energy range 0.2–4.5 keV correcting the luminosity $L_{0.3-8 \text{ keV}} = \text{counts} \times CF$ by the absorption column density, the galaxy distance, and the energy range. The results are reported in Table 3.

Figure 2 shows the variability factor plotted versus the maximum detected flux and the hardness ratio $(R2 - R1)/(R1 + R2)$ (see Sect. 4.3) for each source. The left column shows the variability factors calculated for sources observed in at least two *XMM-Newton* observations. The right column shows the variability factors calculated for sources observed with *Chandra* and in at least one *XMM-Newton* observation.

Applying a variability significance threshold of $S = 3$, we found 35 variable sources. Like XRBs and AGNs, SSSs can show high variability, and because of their soft spectrum (see Sect. 5.6), they can be distinguished from the other sources: in Fig. 2 (lower panels), SSSs candidates should appear on the left-hand side, while XRBs (characterized by a much harder spectrum) are expected to appear on the right-hand side.

4.2. Spectral analysis

We extracted the X-ray spectra of sources with ≥ 300 counts in the energy range 0.2–12 keV. For each source, we fitted all three EPIC spectra simultaneously with different models: powerlaw, disc-blackbody, thermal plasma model (APEC Smith et al. 2001), and blackbody, using XSPEC (ver. 12.7.0, Arnaud 1996). For the absorption we used the PHABS model.

A good fit with one of the above-mentioned spectral models can be used to classify the sources into one of the following classes of sources:

- X-ray binaries;
- supernova remnants;
- super-soft sources.

In total, we fitted the spectra of 12 sources (see Sect. A).

For sources that are not bright enough for spectral modelling, we only calculated their hardness ratios, as described in Sect. 4.3.

4.3. Hardness-ratio diagrams

We used the hardness-ratio diagrams to separate different classes of sources according to their X-ray properties. They are especially helpful for sources that are too faint, for which spectral fitting is not possible. For each source, we computed four hardness ratios, defined as

$$HR_i = \frac{R_{i+1} - R_i}{R_{i+1} + R_i} \quad \text{for } i = 1, \dots, 4, \quad (1)$$

where R_i are the net source counts in five energy bands. To obtain the best statistics we combined the hardness-ratios of all three instruments.

When a source was detected in more than one observation, we considered the observation with the highest number of counts. Some sources can exhibit different spectral states (which can be correlated with the X-ray flux), resulting in hardness-ratio changes between different observations (see e.g. Done et al. 2007). Therefore, for some of these sources we only considered

Table 3. Variability factors (V_f) with errors of sources observed in at least two *XMM-Newton* observations and in *XMM-Newton* and *Chandra* observations.

<i>XMM-Newton</i>									
Source	Flux max.	V_f	Error V_f	S	Source	Flux max.	V_f	Error V_f	S
2	$(3.05 \pm 1.76) \times 10^{-14}$	3.0	0.6	1.2	104	$(8.29 \pm 3.25) \times 10^{-15}$	1.9	0.6	1.0
3	$(3.00 \pm 0.71) \times 10^{-14}$	3.1	0.2	2.9	107	$(1.36 \pm 0.12) \times 10^{-13}$	1.97	0.12	5.1
4	$(1.65 \pm 0.60) \times 10^{-14}$	1.7	0.4	1.2	108	$(1.79 \pm 0.15) \times 10^{-13}$	1.44	0.10	3.3
7	$(1.13 \pm 0.10) \times 10^{-13}$	7.16	0.09	9.4	109	$(3.43 \pm 0.34) \times 10^{-14}$	2.0	0.4	2.4
9	$(2.22 \pm 0.71) \times 10^{-14}$	1.5	0.3	1.1	110	$(1.79 \pm 0.44) \times 10^{-14}$	2.3	0.4	2.1
12	$(7.31 \pm 1.08) \times 10^{-14}$	3.95	0.14	5.0	111	$(5.91 \pm 1.28) \times 10^{-14}$	6.4	0.2	3.9
15	$(8.04 \pm 1.13) \times 10^{-14}$	3.1	0.2	4.4	113	$(3.05 \pm 1.76) \times 10^{-14}$	3.0	0.6	1.2
16	$(1.41 \pm 0.13) \times 10^{-13}$	10.6	0.3	9.5	114	$(1.27 \pm 0.17) \times 10^{-13}$	2.39	0.18	4.1
17	$(7.23 \pm 1.01) \times 10^{-14}$	2.1	0.2	3.3	116	$(3.32 \pm 0.51) \times 10^{-14}$	2.63	0.15	4.0
19	$(1.86 \pm 0.63) \times 10^{-14}$	1.9	0.3	1.4	118	$(3.41 \pm 1.21) \times 10^{-14}$	3.6	0.4	2.0
20	$(5.31 \pm 1.12) \times 10^{-14}$	3.3	0.2	3.3	119	$(1.64 \pm 0.29) \times 10^{-14}$	1.70	0.17	2.4
25	$(2.62 \pm 0.82) \times 10^{-14}$	1.8	0.3	1.4	121	$(2.82 \pm 0.50) \times 10^{-14}$	1.76	0.17	2.4
26	$(2.85 \pm 0.87) \times 10^{-14}$	1.8	0.3	1.4	122	$(2.21 \pm 0.38) \times 10^{-14}$	1.62	0.17	2.2
33	$(2.64 \pm 0.55) \times 10^{-14}$	1.4	0.3	1.1	123	$(2.76 \pm 0.49) \times 10^{-14}$	1.8	0.3	2.1
37	$(7.96 \pm 0.89) \times 10^{-14}$	8.58	0.11	7.9	126	$(4.84 \pm 0.62) \times 10^{-14}$	1.4	0.2	1.4
40	$(1.39 \pm 0.37) \times 10^{-14}$	1.7	0.5	1.2	129	$(4.96 \pm 0.58) \times 10^{-14}$	3.94	0.11	6.4
41	$(1.82 \pm 0.47) \times 10^{-14}$	2.4	0.4	2.0	131	$(2.26 \pm 0.45) \times 10^{-14}$	2.2	0.4	2.1
50	$(3.50 \pm 0.51) \times 10^{-14}$	2.77	0.14	4.4	133	$(7.64 \pm 0.29) \times 10^{-13}$	2.24	0.06	12.4
51	$(2.20 \pm 0.36) \times 10^{-14}$	1.8	0.3	2.0	135	$(5.26 \pm 1.29) \times 10^{-14}$	3.8	0.2	3.0
53	$(2.43 \pm 0.51) \times 10^{-14}$	1.5	0.3	1.3	136	$(1.57 \pm 0.51) \times 10^{-14}$	1.9	0.5	1.2
55	$(2.15 \pm 0.65) \times 10^{-14}$	2.5	0.3	2.0	140	$(2.39 \pm 0.48) \times 10^{-14}$	1.4	0.3	1.1
56	$(2.09 \pm 0.69) \times 10^{-14}$	2.2	0.3	1.7	143	$(1.50 \pm 0.39) \times 10^{-14}$	2.0	0.3	1.9
60	$(7.24 \pm 1.09) \times 10^{-14}$	1.46	0.19	1.8	144	$(9.08 \pm 3.86) \times 10^{-15}$	2.6	0.8	1.2
61	$(7.25 \pm 0.64) \times 10^{-14}$	4.28	0.08	8.6	145	$(1.92 \pm 0.56) \times 10^{-14}$	2.0	0.3	1.7
62	$(1.75 \pm 0.40) \times 10^{-14}$	1.7	0.3	1.6	153	$(3.52 \pm 0.43) \times 10^{-14}$	1.6	0.2	1.9
64	$(3.74 \pm 1.14) \times 10^{-14}$	2.5	0.4	1.9	154	$(1.08 \pm 0.12) \times 10^{-13}$	6.41	0.11	7.5
65	$(1.25 \pm 0.11) \times 10^{-13}$	3.90	0.15	7.8	155	$(4.55 \pm 0.58) \times 10^{-14}$	3.61	0.12	5.7
67	$(8.92 \pm 2.93) \times 10^{-15}$	2.4	0.5	1.6	157	$(3.34 \pm 0.66) \times 10^{-14}$	3.46	0.19	3.6
69	$(3.95 \pm 0.52) \times 10^{-14}$	3.13	0.13	5.1	160	$(8.04 \pm 1.13) \times 10^{-14}$	12.4	0.4	6.4
75	$(1.46 \pm 0.36) \times 10^{-14}$	1.7	0.5	1.1	162	$(1.97 \pm 0.56) \times 10^{-14}$	2.3	0.5	1.7
79	$(3.99 \pm 0.58) \times 10^{-14}$	1.4	0.2	1.5	163	$(1.40 \pm 0.50) \times 10^{-14}$	1.6	0.4	1.1
80	$(3.47 \pm 0.41) \times 10^{-14}$	1.53	0.11	2.9	166	$(1.96 \pm 0.39) \times 10^{-14}$	1.68	0.19	2.0
81	$(5.58 \pm 0.94) \times 10^{-14}$	2.5	0.3	3.0	171	$(7.03 \pm 0.98) \times 10^{-14}$	3.74	0.13	5.3
87	$(1.55 \pm 0.18) \times 10^{-13}$	1.31	0.13	1.9	172	$(3.32 \pm 0.68) \times 10^{-14}$	2.1	0.2	2.5
89	$(1.40 \pm 0.23) \times 10^{-14}$	2.1	0.5	1.8	173	$(3.95 \pm 0.55) \times 10^{-14}$	3.13	0.13	4.9
90	$(1.34 \pm 0.04) \times 10^{-12}$	1.35	0.03	8.1	177	$(5.01 \pm 0.83) \times 10^{-14}$	2.2	0.4	2.6
93	$(2.78 \pm 0.17) \times 10^{-13}$	16.42	0.06	15.6	183	$(2.71 \pm 0.60) \times 10^{-14}$	1.9	0.2	2.1
94	$(1.73 \pm 0.59) \times 10^{-14}$	1.9	0.3	1.4	184	$(2.83 \pm 0.60) \times 10^{-14}$	1.6	0.2	1.8
98	$(4.01 \pm 0.51) \times 10^{-14}$	3.18	0.12	5.4	186	$(2.44 \pm 0.74) \times 10^{-14}$	2.1	0.3	1.7
99	$(1.47 \pm 0.28) \times 10^{-13}$	15.29	0.18	5.0	187	$(1.78 \pm 0.63) \times 10^{-14}$	1.7	0.4	1.2
103	$(1.21 \pm 0.15) \times 10^{-13}$	12.78	0.12	7.2	189	$(7.96 \pm 0.89) \times 10^{-14}$	8.58	0.11	7.9
<i>Chandra</i> and <i>XMM-Newton</i>									
Source	Flux max.	V_f	Error V_f	S	Source	Flux max.	V_f	Error V_f	S
55	$(2.15 \pm 0.65) \times 10^{-14}$	3.3	0.3	2.3	97	$(1.30 \pm 0.12) \times 10^{-13}$	2.79	0.10	6.6
60	$(7.24 \pm 1.09) \times 10^{-14}$	2.35	0.16	3.8	98	$(4.01 \pm 0.51) \times 10^{-14}$	3.18	0.12	5.4
69	$(3.95 \pm 0.52) \times 10^{-14}$	3.13	0.13	5.1	99	$(1.47 \pm 0.28) \times 10^{-13}$	15.29	0.18	5.0
76	$(1.29 \pm 0.60) \times 10^{-14}$	4.5	0.5	1.7	106	$(4.21 \pm 0.52) \times 10^{-14}$	1.28	0.13	1.7
79	$(3.99 \pm 0.58) \times 10^{-14}$	1.4	0.2	1.5	107	$(1.36 \pm 0.17) \times 10^{-13}$	1.97	0.12	5.1
80	$(3.47 \pm 0.41) \times 10^{-14}$	1.53	0.11	2.9	108	$(1.79 \pm 0.15) \times 10^{-13}$	1.44	0.10	3.3
81	$(5.58 \pm 0.94) \times 10^{-14}$	2.5	0.3	3.0	109	$(3.43 \pm 0.34) \times 10^{-14}$	4.02	0.14	7.4
84	$(1.95 \pm 0.42) \times 10^{-14}$	2.7	0.3	2.8	114	$(1.27 \pm 0.17) \times 10^{-13}$	2.39	0.18	4.1
87	$(1.55 \pm 0.18) \times 10^{-13}$	1.35	0.11	2.2	116	$(3.32 \pm 0.51) \times 10^{-14}$	20.8	0.3	6.2
88	$(1.03 \pm 0.33) \times 10^{-14}$	4.6	0.4	2.5	125	$(7.23 \pm 0.27) \times 10^{-15}$	5.3	0.5	2.2
92	$(3.74 \pm 0.19) \times 10^{-14}$	2.7	0.4	4.3	129	$(4.96 \pm 0.58) \times 10^{-14}$	3.94	0.11	6.4
95	$(2.00 \pm 0.44) \times 10^{-14}$	1.9	0.2	2.0					

Notes. Table also includes maximum fluxes and errors in the energy range 0.2–4.5 keV in units $\text{erg cm}^{-2} \text{s}^{-1}$, and the significance of the difference S .

a state by adopting the highest number of counts when determining the hardness ratio. This approach allowed us to obtain the hardness ratios with small uncertainties for bright sources

in their bright states. However, one has to be aware that if a source changes its state, the hardness-ratio may change as well. For fainter sources (with hardness ratio uncertainties $\gtrsim 0.2$), the

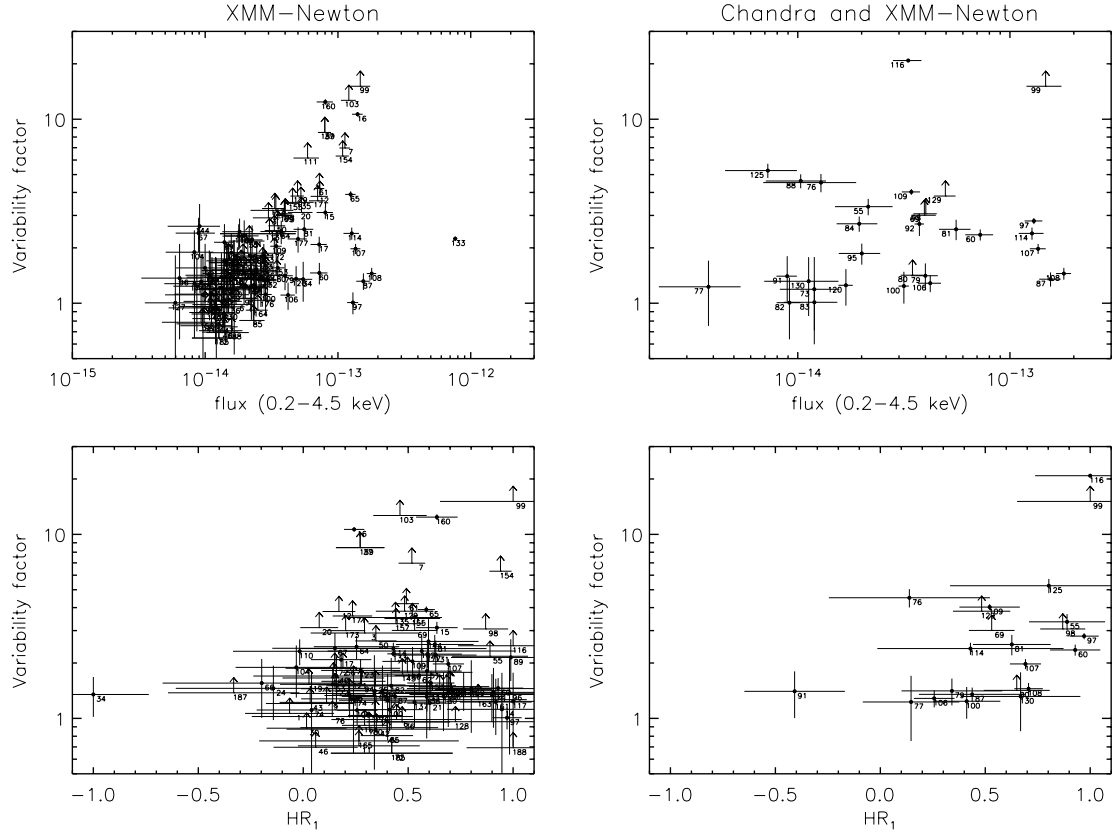


Fig. 2. Left panels: variability factor as a function of the maximum flux (upper panel) and hardness ratio HR_1 (bottom panel) based on *XMM-Newton* observations. Right panels: variability factor as a function of the maximum flux (upper panel) and hardness ratio HR_1 (bottom panel) based on *XMM-Newton* and *Chandra* observations. The lower limits of the variability factors are marked as arrows.

hardness ratios are not sensitive to changes of the state of the source within uncertainties. The hardness ratios calculated for each source are reported in Table B.1.

Figure 3 shows the hardness ratios of sources with errors smaller than 0.3, detected in the field of view of M83. We plotted sources classified as XRBs, SNRs, SSSs, ultra-luminous X-ray sources (ULXs), foreground stars, and background objects (see Sect. 5) with different symbols. On the same plot we also overlaid grids of hardness ratios calculated for different spectral models: three absorbed powerlaws with photon-index $\Gamma = 1, 2, 3$ (XRBs in hard state), two absorbed disc-blackbody models with temperatures at the inner disc radius of $kT_{\text{in}} = 0.5$ and 1 keV (XRBs in soft state), four thermal plasma models APEC with temperatures $kT_{\text{aptec}} = 0.2, 0.5, 1, 1.5$ keV (SNRs), and two blackbody models with temperatures $kT_{\text{bb}} = 50$ and 100 eV (SSSs, see Sect. 5.6). The column densities range from $N_{\text{H}} = 10^{20} \text{ cm}^{-2}$ to $N_{\text{H}} = 10^{24} \text{ cm}^{-2}$.

5. Source classification

We cross-correlated the list of sources observed with *XMM-Newton* with existing catalogues. For this purpose we used X-ray (Trinchieri et al. 1985; Ehle et al. 1998; Immler et al. 1999; SW03; Di Stefano & Kong 2003), optical (Blair & Long 2004; Dopita et al. 2010; Jones et al. 2004; Rumstay & Kaufman 1983; USNO-B1, Monet et al. 2003), radio (Maddox et al. 2006; Cowan et al. 1994; Condon et al. 1998), and infrared (2MASS, Skrutskie et al. 2006) catalogues.

We considered two sources as associated to each other if their positions were closer than the $3\times$ combined statistical errors. The optical counterparts of several X-ray sources cannot be

determined uniquely. In such cases we assumed as counterpart the brightest optical object within the error circle. The cross-correlations are reported in Table B.2.

We used the previous classifications in X-rays and other wavelengths and the methods of classification described in Sects. 4.1 (X-ray variability), 4.2 (spectral analysis), and 4.3 (hardness ratios), to identify and classify sources as background objects, foreground stars, XRBs, SNRs, SSSs, and ULXs.

In this section we describe the observational properties for each class of sources and define the classification criteria.

5.1. Foreground stars

X-ray observations of nearby galaxies are contaminated by foreground stars, which have X-ray luminosities ranging from $\sim 10^{26}$ to $\sim 10^{30} \text{ erg s}^{-1}$ for stars of spectral type F to M, and $\sim 10^{29}$ to $\sim 10^{34} \text{ erg s}^{-1}$ for stars of spectral types O and B (Vaiana et al. 1981; Rosner et al. 1985). Stars of spectral classes F to M emit X-rays because of the intense magnetic fields that form a corona, in which the plasma is heated to temperatures of about $\sim 10^6$ – 10^8 K (e.g. Güdel 2002). A mechanism proposed to explain the X-ray emission from stars of spectral types O–B is the formation of shocks in the coronal regions due to the instability of the wind-driven mechanism (see Puls et al. 2008 and references therein). In A-type stars, none of the above mechanisms for X-ray emission can operate efficiently. Therefore, A-type stars are expected to be weak X-ray sources (Schröder & Schmitt 2007) and only very few have been observed in X-rays (see e.g. Robrade & Schmitt 2010; Schröder et al. 2008).

The X-ray spectra of foreground stars are relatively soft and can be described by models of optically thin plasma in

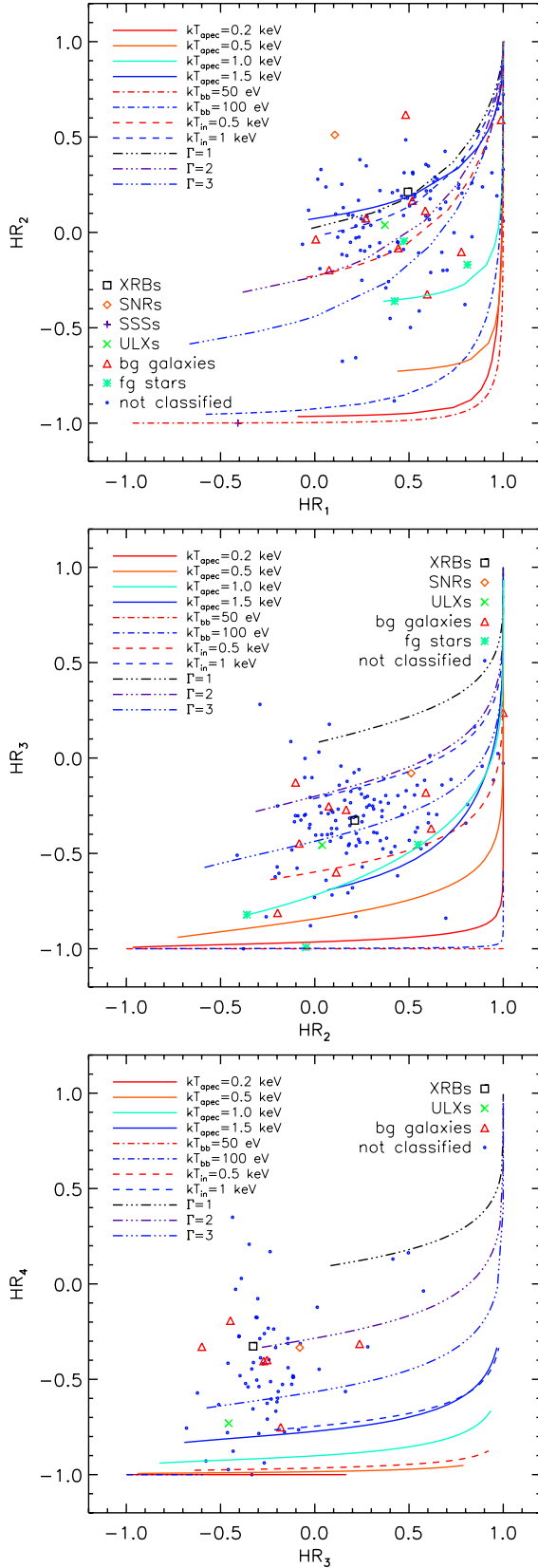


Fig. 3. Hardness-ratio diagrams of sources with error-bars smaller than 0.3. Black squares are sources classified as XRBs (Sect. 5.4), orange diamonds are SNRs (Sect. 5.5), violet plus signs are SSSs (Sect. 5.6), green crosses are ULXs (Sect. 5.8), cyan stars are foreground stars (Sect. 5.1), red triangles are background sources (Sect. 5.2), and blue circles are sources not classified. The lines are the hardness ratios calculated for different spectral models and column densities, as described in Sect. 4.3.

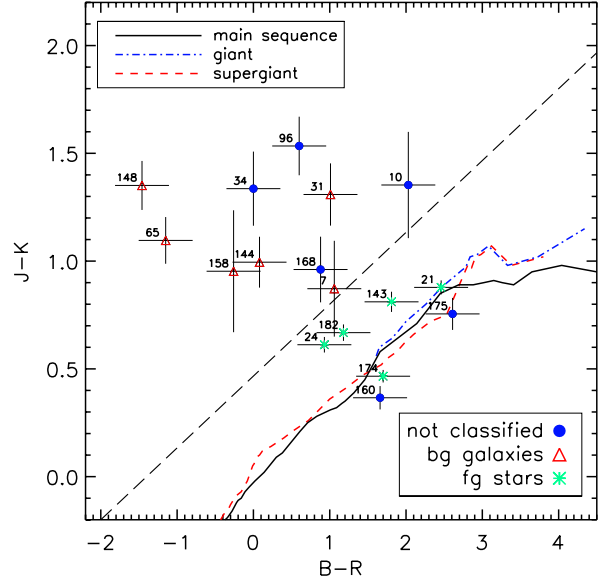


Fig. 4. Colour-colour diagram of *XMM-Newton* sources with optical (USNO-B1) and infrared (2MASS) counterparts. Sources located below the black dashed line are very likely foreground stars.

collisional equilibrium (e.g. Raymond & Smith 1977) with temperatures ranging from 10^6 to 10^7 K. A common method to distinguish stars from other X-ray sources is comparing the X-ray-to-optical flux ratio, as suggested by Maccacaro et al. (1988):

$$\log_{10}(f_x/f_{\text{opt}}) = \log_{10}(f_x) + \frac{m}{2.5} + 5.37, \quad (2)$$

where m is the visual magnitude m_v . In the USNO-B1 catalogue the red and blue magnitudes are given, thus we assumed $m_v \approx (m_{\text{red}} + m_{\text{blue}})/2$. We used the blue magnitude m_{blue} as magnitude m when the red magnitude was not available.

For each X-ray source with an optical counterpart, we distinguished foreground stars from other sources by plotting X-ray-to-optical flux ratios over the hardness ratios HR_2 and HR_3 (Fig. 5). The X-ray-to-optical flux ratios and the hardness ratios differ significantly between different classes of sources.

The soft X-ray flux of early-type stars (OB type) scales with $f_x \approx 10^{-7} f_{\text{opt}}$ (Kudritzki & Puls 2000 and references therein), while the ratio f_x/f_{opt} of late-type stars (F to M) usually ranges from 10^{-6} to 10^{-1} (e.g. Krautter et al. 1999). In contrast, sources such as SNRs, SSSs, and XRBs radiate mainly in X-rays.

We also used optical and near-infrared magnitudes and colours to classify foreground stars (Figs. 4 and 6). Figure 4 is the colour-colour diagram for *XMM-Newton* sources with optical (USNO-B1) and infrared (2MASS) counterparts. Lines show the expected $(B-R)$ and $(J-K)$ colours for main-sequence, giant, and supergiant stars belonging to the Milky Way. We obtained these lines using intrinsic colours calculated by Johnson (1966). Stars located at the Galactic latitude of M 83 ($b \approx 32^\circ$) have on average a colour excess per kiloparsec of $E(B-V) = 0.05 \pm 0.05 \text{ mag kpc}^{-1}$ (Gottlieb & Upson 1969). Therefore, the colour excesses $E(J-K)$ and $E(B-R)$ are negligible compared to the optical and infrared magnitude uncertainties (Schild 1977).

Figures 4 and 6 allow to separate foreground stars from other classes of sources. Foreground stars are brighter in R than background objects or members of M 83, and sources with $J-K \lesssim 1.0$ and $B-R \lesssim 2.0$ are most likely foreground stars.

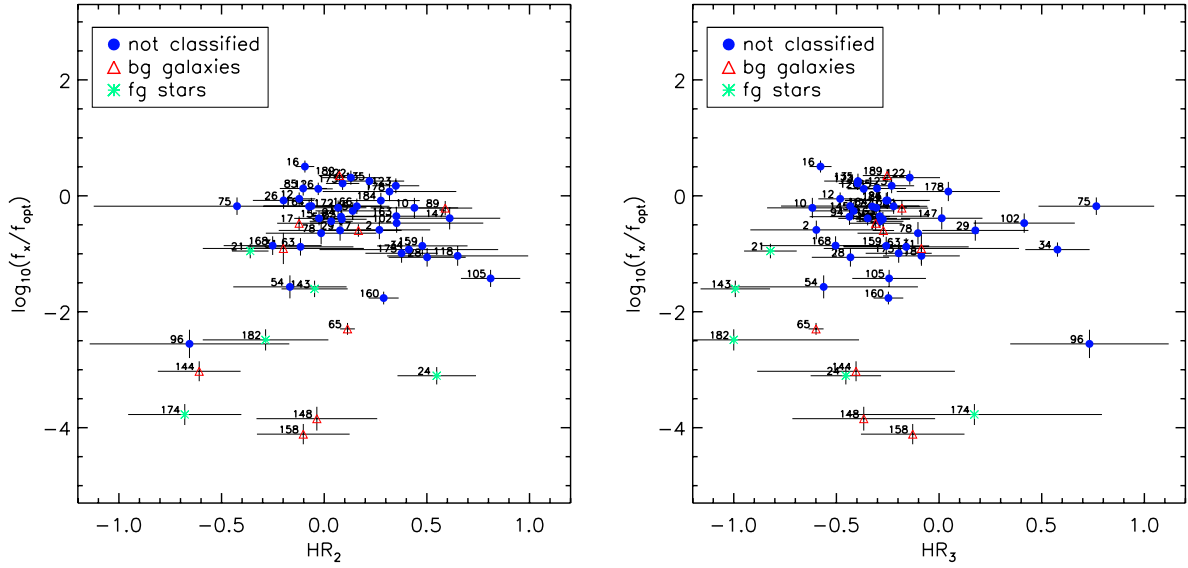


Fig. 5. Flux ratio $\log(f_x/f_{\text{opt}})$ over hardness ratios HR_2 and HR_3 .

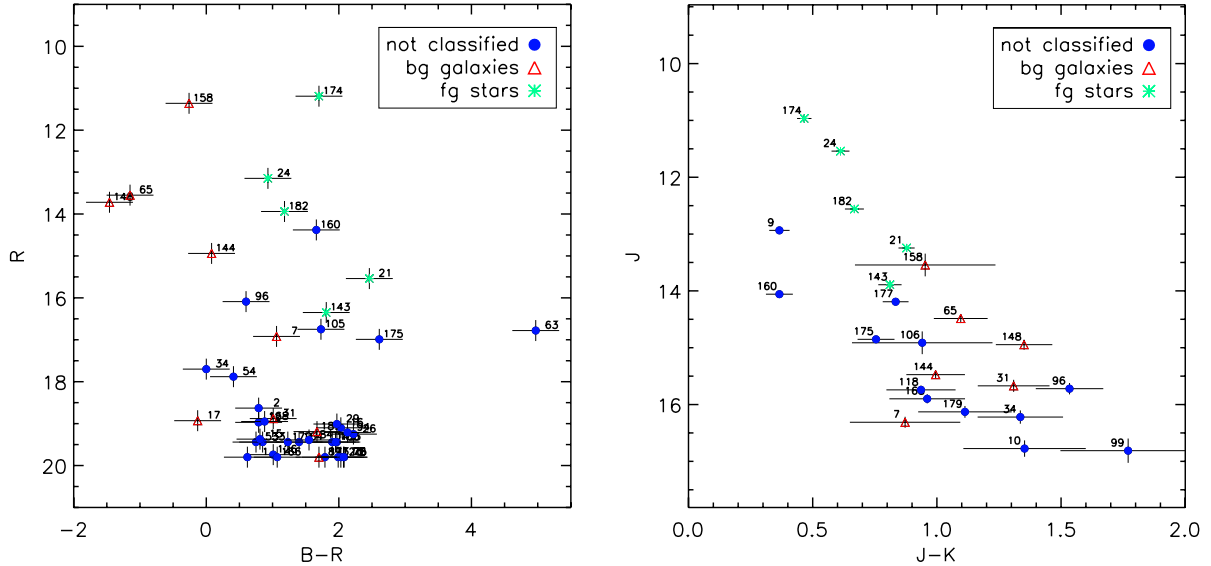


Fig. 6. Colour-magnitude diagrams of *XMM-Newton* sources correlating with sources in the USNO-B1 (left panel) and 2MASS (right panel) catalogues.

From previous considerations, we classified foreground stars when these conditions were met:

- $\log(f_x/f_{\text{opt}}) \lesssim -1$;
- $HR_2 \lesssim 0.3$;
- $HR_3 \lesssim -0.4$;
- $J - K \lesssim 1.0$;
- $B - R \lesssim 2.0$.

The five sources classified as foreground star candidates are reported in Table 4. A detailed discussion of the identification and classification of foreground stars is provided in Sects. A.1 and A.2.

5.2. Background objects

The identification of AGNs, normal galaxies, and galaxy clusters is based on SIMBAD and NED correlations, and is confirmed if there is an optical counterpart in the 2nd Digitized Sky Survey (DSS2) image. New classifications are based on the radio counterpart and hardness ratio $HR_2 \geq -0.4$ (Pietsch et al. 2004).

Table 4. M83 X-ray sources and their associated candidate sources in our Galaxy.

No.	RA (J2000)	Dec (J2000)	USNO-B1	<i>B</i> mag.	<i>R</i> mag.
21	13 36 18.73	–30 01 38.1	0599-0299962	18.0	15.5
24	13 36 19.95	–29 51 08.3	0601-0298625	14.1	13.2
143	13 37 27.29	–29 55 45.5	0600-0300561	18.2	16.4
174	13 37 44.79	–30 07 49.2	0598-0301638	12.9	11.2
182	13 37 57.77	–30 01 40.6	0599-0300696	15.1	13.9

We identified nine sources as background galaxies and AGNs (sources No. 7, 17, 31, 65, 83, 89, 144, 148, see Table 5). We found radio counterparts of the sources Nos. 20, 37, 189 and classified them as AGN candidates for the first time (see Sect. A.3). Based on the $\log N - \log S$ calculated by Cappelluti et al. (2009) (see Sect. 6.2), about 40 observed sources (with a 2–10 keV flux $F_x > 10^{-14}$ erg cm $^{-2}$ s $^{-1}$) are expected to be background objects in each *XMM-Newton* observation of

Table 5. X-ray sources identified and classified as galaxies or AGNs and their counterparts or previous X-ray classifications.

No.	RA (J2000)	Dec (J2000)	Name (SIMBAD)
Identifications:			
7	13 36 04.66	−30 08 30.8	QSO B1333–298
17	13 36 15.42	−29 57 58.2	[I1999] 5 ³
31	13 36 28.13	−29 42 27.9	2MASS J13362821–2942266
65	13 36 45.78	−29 59 13.0	6dFGS gJ133645.8–295913
83	13 36 58.26	−29 51 04.3	[MCK2006] 28 ¹
89	13 36 59.68	−30 00 58.8	[BRK2009] 7 ²
144	13 37 27.46	−30 02 28.3	6dFGS gJ133727.5–300228
148	13 37 29.36	−29 50 27.4	6dFGS gJ133729.5–295028
158	13 37 32.94	−29 51 01.2	ESO 444–85
New classifications:			
20	13 36 18.21	−30 15 00.5	NVSS J133618–301459
37	13 36 30.53	−30 16 57.0	NVSS J133630–301651
189	13 38 05.57	−29 57 45.4	NVSS J133805–295748

References. ⁽¹⁾ Maddox et al. (2006); ⁽²⁾ Bresolin et al. (2009); ⁽³⁾ Immler et al. (1999).

Table 1. From a comparison with other works (e.g. Misanovic et al. 2006), we expect a large difference between the predicted number of background objects from background surveys and the number of identified/classified background objects in an *XMM-Newton* observation. This difference is due to the difficulty in classifying sources which, because of their distance, are too faint (and therefore provide little information) to be classified with the methods at our disposal.

5.3. Nuclear sources

We detected two bright sources in the nuclear region of M 83 with the source detection procedure: sources No. 92 and No. 95. They are separated by $\sim 6.3''$ and are the brightest sources detected with *XMM-Newton* in M 83 ($F_{\text{No. 90}} = [1.03 \pm 0.25] \times 10^{-12} \text{ erg cm}^{-2} \text{ s}^{-1}$; $F_{\text{No. 93}} = [2.59 \pm 0.15] \times 10^{-13} \text{ erg cm}^{-2} \text{ s}^{-1}$; 0.2–12 keV, assuming an absorbed powerlaw spectrum with index 1.8 and a foreground Galactic absorption of $N_{\text{H}} = 3.69 \times 10^{20} \text{ cm}^{-2}$). The two nuclear sources coincide with ~ 18 *Chandra* sources and the bright diffuse emission of the starburst nucleus, not resolved by *XMM-Newton* because of its high PSF, which causes source confusion in crowded regions, such as the nuclear region of M 83.

5.4. X-ray binaries

We classified sources as XRBs if the X-ray spectra or hardness ratios were compatible with the typical spectra of XRBs and we detected a flux periodicity.

We identified two X-ray binaries (Nos. 81 and 120), previously classified by SW03 using *Chandra* observations (Sect. A.4).

5.5. Supernova remnants

We assume that the X-ray spectra of SNRs are well described by the thermal plasma model APEC (Smith et al. 2001), with temperatures ranging from 0.2 to 1.5 keV. At this distance we are unable to resolve an SNR or to verify a more detailed spectral model assuming, e.g., a non-equilibrium ionisation.

We classified an X-ray source as SNR if $HR_1 > 0.1$, $HR_2 < -0.4$, the source was not a foreground star, and did not show a significant variability (Pietsch et al. 2004).

We identified the source No. 79 as source [SW03] 27, classified as a young SNR candidate by SW03 (Sect. A.5).

SN1957D. Long et al. (2012) reported the first detection of SN1957D in X-rays with *Chandra*. The source shows a luminosity of $1.7 \times 10^{37} \text{ erg cm}^{-2} \text{ s}^{-1}$ ($d = 4.61 \text{ Mpc}$, Saha et al. 2006; 0.3–8 keV), and the spectrum is well modelled with an absorbed powerlaw with an index ~ 1.4 , a foreground Galactic absorption of $N_{\text{H}} = 4 \times 10^{20} \text{ cm}^{-2}$ and an intrinsic column density of $N_{\text{H}} = 2 \times 10^{22} \text{ cm}^{-2}$. We did not detect SN1957D in the *XMM-Newton* observations. In observation 1 the source is located near to the centre of the field of view, and in the other two observations the source is located at the edge of the field of view. Assuming the spectral parameters found by Long et al. (2012), we calculated a 3σ upper-limit in observation 1 of $\sim 2.4 \times 10^{-14} \text{ erg cm}^{-2} \text{ s}^{-1}$ (0.2–12 keV), corresponding to a luminosity of $\sim 5.8 \times 10^{37} \text{ erg s}^{-1}$, well above the luminosity detected by Long et al. (2012).

5.6. Super-soft sources

Super-soft sources are a class of sources that are believed to be binary systems containing a white dwarf. The white dwarf accretes matter from a Roche-lobe-filling companion at high rates ($\dot{M}_{\text{acc}} \sim 10^{-7} M_{\odot} \text{ yr}^{-1}$), which leads to quasi-steady nuclear burning on its surface (see e.g. van den Heuvel et al. 1992). SSSs show soft spectra with blackbody temperatures of 15–150 eV and X-ray luminosities ranging from $\sim 10^{35} \text{ erg s}^{-1}$ to $10^{38} \text{ erg s}^{-1}$ (Di Stefano & Kong 2003; Kahabka & van den Heuvel 1997). An additional harder component, due to interactions of the radiation with matter near to the white dwarf or wind interactions can be observed (Di Stefano & Kong 2003). Moreover, SSSs are often observed as transient X-ray sources (see Greiner 2000). Other classes of sources with soft spectra can be confused with SSSs. For example, some X-ray pulsars observed outside the beam of the pulsed radiation can show a soft ($\sim 30 \text{ eV}$) component (Hughes 1994; Di Stefano & Kong 2003). Moreover, stripped cores of giant stars can be classified as SSSs (Di Stefano et al. 2001).

As our classification criteria, we assumed blackbody temperatures of $kT_{\text{bb}} \leq 100 \text{ eV}$ (in agreement with the selection procedure proposed by Di Stefano & Kong 2003) and hardness ratios that do not overlap with those of other classes of sources. These criteria are an $HR_1 \lesssim 0$ and $HR_2 - EHR_2 < -0.9$. We classified a source as SSS only if both criteria are fulfilled.

We identified source No. 91 as source M 83–50, classified as an SSS candidate by Di Stefano & Kong (2003) using *Chandra* observations (Sect. A.6).

5.7. Hard sources

Hard sources show hard X-ray spectra (or hard HRs, see Table 5 in Pietsch et al. 2004). Using their spectral properties and hardness ratios, we classified five hard sources (Nos. 16, 61, 103, 126, and 153; see Sect. A.8.1) and we identified 11 hard sources (Nos. 60, 80, 92, 97, 99, 106, 107, 108, 114, 116, 129; see Sect. A.8.2).

5.8. Ultra-luminous X-ray sources

ULXs are pointlike non-nuclear sources with X-ray luminosities in excess of the Eddington limit ($L_{\text{Edd}} \approx 10^{39} \text{ erg s}^{-1}$) for a stellar

mass black-hole (see e.g. Feng & Soria 2011). They are usually located in active star-forming environments (Miller & Colbert 2004), and their nature is still unclear; recent studies indicate that ULXs are a heterogeneous sample of objects (e.g. Gladstone 2010).

Several models have been proposed to explain the high X-ray luminosity of ULXs, but there are three models that are often used for this class of sources. The first model requires that ULXs are intermediate-mass black-hole systems (IMBHs) with masses $M \sim 10^2\text{--}10^4 M_\odot$, accreting at sub-Eddington rates (e.g. Colbert & Mushotzky 1999). The other models assume that ULXs are stellar-mass black holes (with masses $M \lesssim 100 M_\odot$) in a super-Eddington accretion regime (Poutanen et al. 2007) or with beamed radiation (see e.g. King 2009).

We identified ULX No. 133, discovered by Trinchieri et al. (1985) with *Einstein* (source H2), and previously observed in X-rays with ROSAT by Ehle et al. (1998) and Immler et al. (1999) (see Sect. A.7).

6. X-ray luminosity functions

For each observation, we calculated the XLFs in the energy range 2–10 keV excluding the softer bands to reduce the effect of incompleteness of the observed source sample due to absorption. Moreover, from an XLF calculated in this energy band, it is possible to easily subtract the contribution of the $\log N - \log S$ of the AGNs, which was calculated from several surveys performed by *XMM-Newton* and *Chandra* (see Sect. 6.2).

We considered for XLFs only sources with a detection likelihood greater than 6 in the energy range 2–12 keV. For each source, we converted the count rates to the 2–10 keV fluxes using the ECFs of Table 2 for the energy bands R4 and R5.

We excluded the region inside a circle centred on the nuclear region of M 83 with radius $R = 26''$ from the XLF calculation, where the large PSF of EPIC in a crowded region causes source confusion effects (see Sect. 5.3). Since we were interested in obtaining XLFs of XRBs, we also excluded the sources previously classified as SNRs, SSSs, ULXs, and foreground stars (Sect. 5). For each observation, we calculated the XLFs of sources detected within two regions of M 83: the inner disc inside the D_{25} ellipse, and the outer disc outside the D_{25} ellipse.

6.1. XLFs corrected for incompleteness

The sensitivity of the EPIC instruments depends on the exposure, background, and PSF, which are not uniform across the FOV. Indeed, the exposure time is relatively high at the centre of the FOV and decreases with increasing off-axis angle (vignetting effect). The background, modelled by the task *esplinemap*, decreases with increasing angular distance from the nuclear region of M 83 (due to the diffuse emission in the disc of M 83), and the optical properties of the X-ray telescope introduce a degradation of the PSF with increasing off-axis angle. Therefore, the sensitivity also varies across the observed area, allowing the detection of the brightest sources across the entire observed area, whereas the effective area for the detection of faint sources is smaller. This effect leads to an underestimation of the number of sources observed at the faintest flux levels.

We corrected the XLFs by taking into account the incompleteness effect described above by calculating the *sky coverage function*, which is the effective area covered by the observation as a function of flux. For each observation, we first created the combined sensitivity maps of PN, MOS1, and MOS2

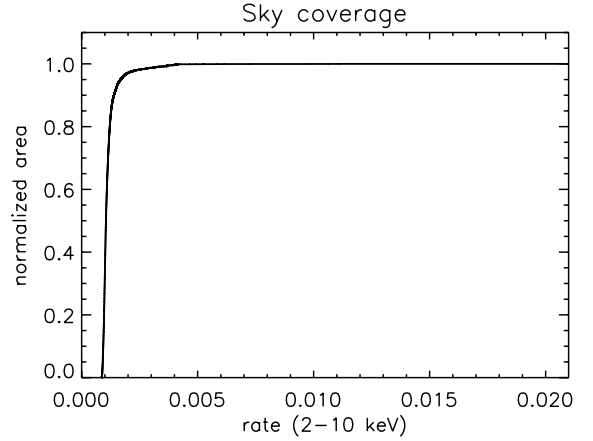


Fig. 7. Sky coverage as a function of the X-ray flux (2–10 keV) for the region inside the D_{25} ellipse (observation 1), calculated excluding the region within the circle centered on the nuclear region of M 83 with radius $R = 26''$.

with the SAS task *esensmap*, which requires as input files the exposure maps, the background images, and the detection masks created by the source detection procedure. We used the sensitivity maps to calculate the sky coverage function for each observation (Fig. 7). The cumulative XLF corrected for incompleteness is given by

$$N(>F_x) = A_{\text{tot}} \sum_{i=1}^{N_s} \frac{1}{\Omega(F_i)}, \quad (3)$$

where $N(>F_x)$ is the number of sources with a flux higher than F_x , weighted by the fraction of the surveyed area $\Omega(F_i)/A_{\text{tot}}$ over which sources with flux F_i can be detected; A_{tot} is the total area of the sky observed by EPIC, $\Omega(F_i)$ is the sky coverage (Fig. 7), and N_s is the total number of the detected sources. Therefore, with Eq. (3), every source is weighted with a factor correcting for incompleteness at its flux. The variance of the source number counts is defined as

$$\sigma^2 = \sum_{i=1}^{N_s} \left(\frac{1}{\Omega_i} \right)^2. \quad (4)$$

6.2. AGN-corrected XLFs

The XLFs obtained in Sect. 6.1 consist of sources belonging to M 83 (XRBs) and AGNs. We subtracted the AGN contribution using the AGN XLF of Cappelluti et al. 2009, who derived the XLFs from the 2 deg² of the XMM-COSMOS survey (Scoville et al. 2007). These authors found that the XLF of AGNs in the energy range 2–10 keV is described by a broken powerlaw:

$$\frac{dN}{dF} = \begin{cases} AF^{-\alpha_1} & F > F_b \\ BF^{-\alpha_2} & F \leq F_b, \end{cases} \quad (5)$$

where $A = BF_b^{\alpha_1 - \alpha_2}$ is the normalisation, $\alpha_1 = 2.46 \pm 0.08$, $\alpha_2 = 1.55 \pm 0.18$, $F_b = (1.05 \pm 0.16) \times 10^{-14} \text{ erg cm}^{-2} \text{ s}^{-1}$, and $A = 413$.

Figure 8 shows the XLFs of sources detected within the D_{25} ellipse and outside, calculated for each *XMM-Newton* observation. Blue lines are the observed XLFs, and black lines are the XLFs corrected for incompleteness. Solid green lines are the AGN XLFs of Eq. (5) with relative uncertainties (dashed green

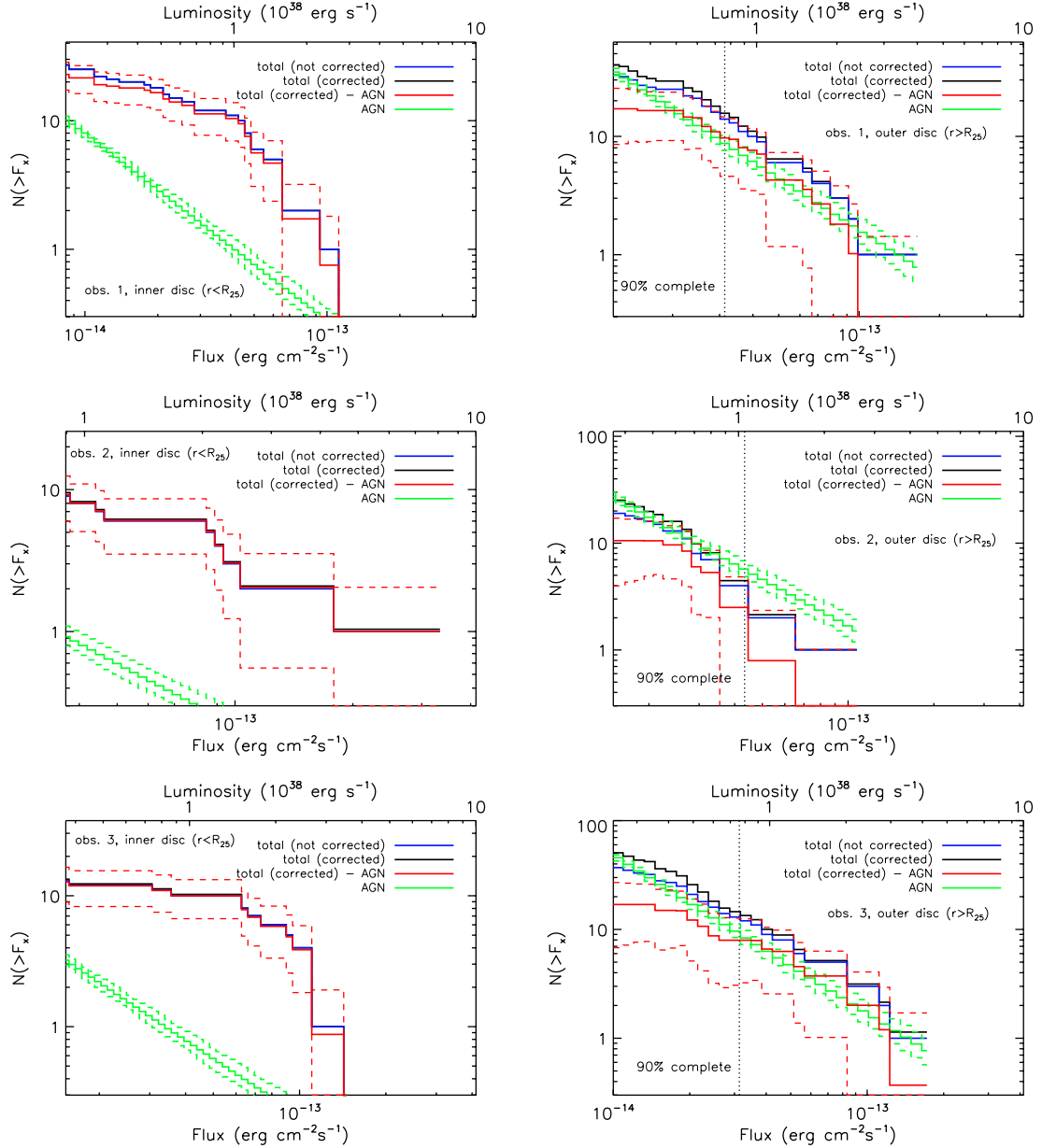


Fig. 8. Cumulative XLFs in the 2–10 keV energy band. Blue lines correspond to the XLFs without the contribution of SNRs, SSSs, ULX, and foreground stars, not corrected for incompleteness. Black lines are the XLFs corrected for incompleteness. Solid green lines are the AGN XLFs of Cappelluti et al. (2009), and dashed green lines are the 90% confidence errors. Solid red lines are the XLFs corrected for incompleteness and AGN-subtracted, and the dashed red lines are the resulting uncertainties.

lines). Solid red lines show the XLFs corrected for incompleteness and AGN-subtracted, and dashed red lines are the 90% confidence errors, obtained from Eq. (4) and the 90% confidence errors of the AGN distribution.

Vertical black lines in the right column of Fig. 8 show the level at which the survey is 90% complete (see Sect. 6.3.2), defined as the flux at which

$$\sum_{i=1}^{N_s} N(F_i) / \sum_{i=1}^{N_s} A_{\text{tot}} / \Omega(F_i) = 0.9.$$

6.3. Fit

We fitted the differential XLFs corrected for incompleteness and AGN-subtracted with a powerlaw:

$$A(F) = kF^\alpha, \quad (6)$$

where k is the normalisation and α the powerlaw index. We also fitted the differential XLFs with a broken powerlaw:

$$A(F) = \begin{cases} kF_b^{\alpha_2 - \alpha_1} F^{\alpha_1} & F > F_b \\ kF^{\alpha_2} & F \leq F_b, \end{cases} \quad (7)$$

where F_b is the break point. The resulting parameters obtained from the fit are reported in Table 6.

6.3.1. Inner disc

From *Chandra* observation, SW03 calculated the XLFs of sources located in the inner region (distance $< 60''$ from the nucleus) and outer region ($60'' < d < R_{25}$) of the optical disc. They found that the inner region sources have a powerlaw luminosity distribution with an differential index of -1.7 , while the luminosity distribution of the outer region sources shows a lack of bright sources above $\sim 10^{38} \text{ erg s}^{-1}$. These authors modelled

Table 6. Best-fitting parameters of the differential XLFs of observations 1, 2, and 3, calculated for sources within and outside the D_{25} ellipse.

	$<R_{25}$		
	Obs. 1	Obs. 2	Obs. 3
	powerlaw ^a		
α	-1.0 ± 0.3	-1.8 ± 0.4	-1.6 ± 1.2
k	$10.4^{+1.8}_{-1.6}$	$11.2^{+5.9}_{-3.9}$	$21.4^{+38.9}_{-13.8}$
χ^2 (d.o.f.)	23.48 (15)	11.74 (5)	9.20 (5)
	broken powerlaw ^b		
α_1	$-3.0^{+0.9}_{-0.2}$	$-2.9^{+0.8}_{-0.2}$	
α_2	$-1.1^{+0.1}_{-0.5}$	$-1.1^{+0.1}_{-0.4}$	
k	$20.9^{+13.0}_{-8.0}$	$37.2^{+48.0}_{-20.9}$	
F_b (10^{-14} erg cm $^{-2}$ s $^{-1}$)	$5.6^{+1.0}_{-0.4}$	$6.5^{+0.8}_{-0.7}$	
χ^2 (d.o.f.)	21.01 (13)	9.17 (3)	
	$> R_{25}$		
	powerlaw ^a		
α	-1.9 ± 0.5	-3.3 ± 1.1	-1.2 ± 0.4
k	$13.4^{+4.7}_{-3.5}$	$8.7^{+3.5}_{-2.5}$	$7.1^{+2.0}_{-1.6}$
χ^2 (d.o.f.)	11.62 (11)	4.41 (5)	8.68 (9)

Notes. For each observation, the best-fitting parameters were obtained using the total XLF corrected for incompleteness and AGN-subtracted. (a) See Eq. (6); (b) see Eq. (7).

the XLF of these sources with a broken powerlaw with a break around $\sim 10^{38}$ erg s $^{-1}$ and differential indices of -1.6 and -2.6 . They explained the XLF of the inner region sources in terms of current starburst activity, while the XLF of the outer region may result from an older population of disc sources mixing with a younger population.

We recall that we cannot study the innermost region because of poor spatial resolution of *XMM-Newton* compared to *Chandra*. We compared the best-fitting parameters of the XLF of the outer region sources ($60'' < d < R_{25}$) obtained by SW03 with those obtained from the *XMM-Newton* analysis (Table 6). In particular, we considered the broken powerlaw fit of sources detected in observation 1. Only during this observation was the whole optical disc of M83 observed. We found that the indices α_1 , α_2 and the break F_b of Eq. (7) agree within the uncertainties with the parameters found by SW03.

Grimm et al. (2003) studied the XLFs of a sample of galaxies and found the probable existence of a universal HMXB XLF (in the luminosity range $\sim 4 \times 10^{36} - 10^{40}$ erg s $^{-1}$), described by a powerlaw with differential slope of -1.6 . They found that the number of HMXBs with $L_x > 2 \times 10^{38}$ erg s $^{-1}$ in a star-forming galaxy is directly proportional to the SFR, and proposed that the number and the total X-ray luminosity of HMXBs can be used to measure the star formation rate of a galaxy. Based on a much larger sample of galaxies, Mineo et al. (2012) found that the properties of populations of HMXBs and their relation with the SFR agree with those obtained by Grimm et al. (2003). We estimated the SFR in the optical disc of M83 using the $N_{\text{HMXBs}} - \text{SFR}$ relation of Mineo et al. (2012):

$$N(>10^{38} \text{ erg s}^{-1}) = 3.22 \times \text{SFR} (M_{\odot} \text{ yr}^{-1}). \quad (8)$$

We assumed that the XLF we used for this calculation provides a good approximation of the HMXB XLF in M83. The contribution of LMXBs to the XLF is negligible for a starburst galaxy such as M83 when $L_x \gtrsim 10^{38}$ erg s $^{-1}$ (Grimm et al. 2003).

Moreover, the contribution of LMXBs to the XLF is minimized by excluding the nuclear region of the galaxy, from which a strong contribution to the total number of LMXBs is expected. Using the XLF of sources detected in observation 1 within the D_{25} ellipse, from Eq. (8) we found an $\text{SFR} \approx 3.1 M_{\odot} \text{ yr}^{-1}$, in agreement with the SFR estimates obtained from observations in other wavelengths (see e.g. Boissier et al. 2005; Dong et al. 2008; Grimm et al. 2003 and references therein).

6.3.2. Outer disc

The XLFs of the outer disc ($d > R_{25}$) show an excess of sources (with respect to the expected number of AGNs) in the luminosity range $\sim 10^{37}$ to $\sim 2 \times 10^{38}$ erg s $^{-1}$ (Fig. 8).

We are interested in calculating the probability of the luminosity distribution of the observed sources to be consistent with the luminosity distribution of Eq. (5) which represents the AGN distribution. Therefore, we compared for each observation the luminosity distribution of the sources detected in the outer disc ($d > R_{25}$) that was not corrected for incompleteness (see Sect. 6) with a distribution of simulated sources over the EPIC FOV obtained from a uniform spatial distribution of sources with a luminosity distribution given by Eq. (5), filtered to exclude sources with a flux below the detection threshold calculated at the position of each source in the sensitivity map. The Kolmogorov-Smirnov test applied to these source samples showed that the probabilities that the luminosity distributions of the observed sources are consistent with the luminosity distribution of AGNs (Eq. (5)) are almost zero, being 0.04% in observation 1, 0.7% in observation 2, and 0.6% in observation 3.

To quantify the probability that the set of X-ray sources located outside the D_{25} ellipse are AGNs (which are expected to be uniformly distributed across the sky) or XRBs (whose distribution should not be uniform, because the position of XRBs should correlate with the arms extending out of the optical disc), we performed a two-dimensional Kolmogorov-Smirnov test (Fasano & Franceschini 1987; Peacock 1983). This test is based on the statistic δ , which in the unidimensional Kolmogorov-Smirnov test represents the largest difference between two cumulative distributions. We applied this test to two data samples:

1. all X-ray sources detected in observation 1 that are located outside the D_{25} ellipse. The number of these sources is $N_1 = 39$;
2. a distribution of simulated sources in the EPIC FOV of observation 1, obtained from a uniform spatial distribution of sources (which represents the uniform spatial distribution of AGNs) modified to take into account the incompleteness effect described in Sect. 6.1. We obtained this spatial distribution of sources as follows. We first generated a uniform spatial distribution of sources with fluxes given by the XLF of AGNs described in Sect. 6.2. Then, we selected sources with flux higher than that corresponding to the position of each source in the sensitivity map. We additionally selected sources with luminosity $> 10^{37}$ erg s $^{-1}$ in the energy range 2–10 keV that are located outside the D_{25} ellipse. With this method, we generated a sample of $N_2 = 10^4$ coordinate pairs (RA, Dec) of sources (see Fig. 9).

From the number of data points N_1 and N_2 of the two data sets, the significance level was calculated from the probability distribution of the quantity

$$Z_n \equiv \delta \sqrt{n}, \quad (9)$$

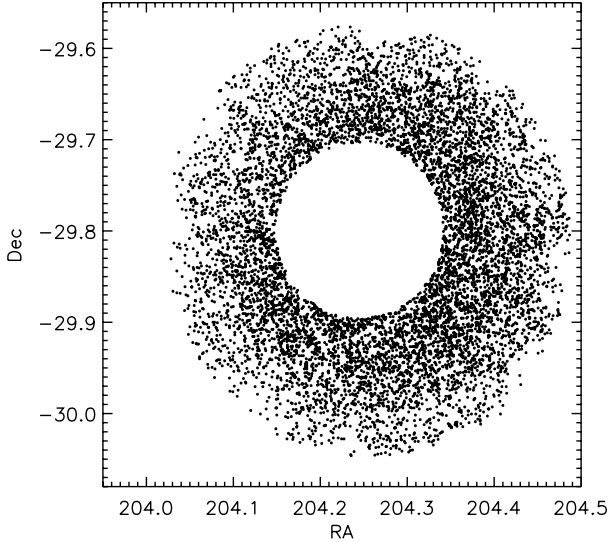


Fig. 9. Sample of 10^4 simulated sources, distributed over the EPIC field of view of observation 1 and located outside the D_{25} ellipse.

where $n = N_1 N_2 / (N_1 + N_2)$. The analytical formula for calculating of the probability that the two data samples come from the same distribution is accurate enough for large data sets with $n > 80$ (Fasano & Franceschini 1987). Since in our case $n \approx 39$, we needed to use Monte Carlo simulations. We generated many synthetic data samples simulating the uniformly distributed AGNs with the same method previously used to calculate sample 2; each of the synthetic data samples has the same number of sources as the observed data set 1 ($N_1 = 39$). For each data set we applied the 2D Kolmogorov-Smirnov test by comparing the synthetic data set with the set of 10^4 sources distributed across the EPIC FOV previously described, then we calculated the quantity Z_n using Eq. (9). The probability of the observed Z_n is given by the fraction of the times the simulated Z_n are larger than the observed Z_n .

Applying this statistical method to our data, we found a probability of 99.5% that the observed sample 1 and the simulated homogeneously distributed sample 2 are significantly different, which suggests a non-uniform distribution of the observed X-ray sources and therefore a possible correlation between the positions of these sources and the extended arms of M 83.

The incompleteness correction given by Eq. (3) is based on the hypothesis that sources are uniformly distributed. However, we have demonstrated that the X-ray sources located outside the D_{25} ellipse have a non-uniform distribution, hence the associated XLFs corrected for incompleteness of Fig. 8 (right column) are not reliable at low luminosities. Therefore we only considered the part of the XLFs with luminosities higher than the level at which the survey is 90% complete (to the right of the vertical black lines in Fig. 8). We found that the 90% complete XLFs of observations 1 and 3 (for which we have enough data points to find a good fit) are well fitted with a powerlaw with differential slopes $\alpha = -2.2 \pm 0.5$ (observation 1), and $\alpha = -1.7 \pm 0.4$ (observation 3), which are consistent with each other within errors. These are also consistent with the AGN slope of Cappelluti et al. (2009).

Assuming that the spatial distribution of AGNs and their number density are not subject to strong fluctuations on small angular scales corresponding to different directions in the M 83 field, the observed excess of sources (with respect to the AGN distribution) in the luminosity range $\sim 10^{37}$ to $\sim 2 \times 10^{38}$ erg s $^{-1}$

(Fig. 8) can probably be ascribed to a population of XRBs located in the outer disc of M 83. The recent star-forming activity discovered by GALEX in this region indicates that a large portion of the observed X-ray sources are HMXBs. However, the observed XLF slope is steeper than the slope of the universal HMXB XLF inferred by Grimm et al. (2003). A possible explanation for the difference between the two slopes could be that the observed XLFs are the result of a mix of XRB populations formed after starbursts of different ages. An alternative explanation is that the mass distribution of the population of stars in the low-density regions of the outer disc of M 83 is described by a truncated initial mass function (IMF), whose existence was proposed to explain the production of fewer high-mass stars (compared to the standard IMF) in low-density environments (see e.g. Krumholz & McKee 2008; Meurer et al. 2009). The universality of the IMF is still a matter of debate (Bastian et al. 2010); in this context, a recent Subaru H α observation of the outer disc of M 83 revealed O stars even in small clusters ($M \lesssim 10^3 M_\odot$), which supports the hypothesis that the IMF is not truncated in low-density environments (Koda et al. 2012).

7. Summary

We presented an analysis of three *XMM-Newton* observations of M 83. We performed the source detection procedure separately for images of each observation, and we obtained a catalogue containing 189 sources.

Based on cross-correlations with other catalogues we identified counterparts for 103 sources, 12 of which were identified or classified as background objects and 5 as foreground stars (one as candidate CV). We performed spectral analysis of the sources with the largest number of counts, as well as studies of the X-ray variability and the hardness ratio diagrams. The spectral analysis of ULX No. 133 in observations 2 and 3 showed good fits with the standard IMBHs model as well as with accreting stellar-mass black-hole model, in agreement with the results obtained by Stobbart et al. (2006) from observation 1.

In Sect. 6 we presented the XLFs of sources in the 2–10 keV energy band, within and outside the D_{25} ellipse. We corrected the XLFs for incompleteness and subtracted the contribution of background AGNs from the total XLF to obtain the XLFs of XRBs. The XLF of the optical disc is well fitted with a powerlaw or a broken powerlaw, while the XLF of the outer disc is well fitted with a simple powerlaw. The broken powerlaw fit parameters agree (within the uncertainties) with the parameters found by SW03 with *Chandra*. From the *XMM-Newton* XLF, we obtained an $SFR \approx 3.1 M_\odot \text{ yr}^{-1}$ in the optical disc of M 83, which agree with previous estimates obtained in other wavelengths.

The XLFs of these sources show an excess of sources (compared to the AGNs distribution) in the luminosity range $\sim 10^{37}$ to $\sim 2 \times 10^{38}$ erg s $^{-1}$. The application of the Kolmogorov-Smirnov test to the X-ray sources detected outside the D_{25} ellipse allowed us to find that this population of sources is significantly different from the population of background AGNs, which is supposed to have a homogeneous distribution. These results led us to suggest that a part of the X-ray sources observed outside the D_{25} ellipse belongs to the outer disc of M 83. The 90% complete XLFs of the outer disc are well fitted with a simple powerlaw with differential slope $\alpha = -2.2 \pm 0.5$ (observation 1), and $\alpha = -1.7 \pm 0.4$ (observation 3) steeper than the universal HMXB XLF discovered by Grimm et al. (2003). We proposed as a possible origin for the steep slope of the observed XLF that the observed XLFs are the result of a mix of XRB populations of different ages, or, as an alternative explanation, that the IMF in the low-density

regions of the outer disc of M 83 is truncated, as previously suggested by e.g. [Krumholz & McKee \(2008\)](#) and [Meurer et al. \(2009\)](#) to explain the low production of high-mass stars in low-density environments. Additional X-rays and UV observations of the outer disc of M 83, analysed with most effective methods such as the one used by [Bodaghee et al. \(2012\)](#) to measure the spatial cross-correlation of HMXBs and OB star-forming complexes in the Milky Way, will be fundamental to confirm our hypothesis.

Acknowledgements. We thank the referee Eric M. Schlegel for constructive comments, which helped to improve the manuscript. This research is funded by the Deutsche Forschungsgemeinschaft through the Emmy Noether Research Grant SA 2131/1. This research has made use of the SIMBAD database, operated at CDS, Strasbourg, France, and of the NASA/IPAC Extragalactic Database (NED), which is operated by the Jet Propulsion Laboratory, California Institute of Technology, under contract with the National Aeronautics and Space Administration. This publication has made use of data products from the Two Micron All Sky Survey, which is a joint project of the University of Massachusetts and the Infrared Processing and Analysis Center, funded by the National Aeronautics and Space Administration and the National Science Foundation. This research has made use of SAOImage DS9, developed by Smithsonian Astrophysical Observatory.

References

- Arnaud, K. A. 1996, in *Astronomical Data Analysis Software and Systems V*, eds. G. H. Jacoby, & J. Barnes, ASP Conf. Ser., 101, 17
- Bastian, N., Covey, K. R., & Meyer, M. R. 2010, *ARA&A*, 48, 339
- Bigiel, F., Leroy, A., Seibert, M., et al. 2010, *ApJ*, 720, L31
- Blair, W. P., & Long, K. S. 2004, *ApJS*, 155, 101
- Blair, W. P., Winkler, P. F., & Long, K. S. 2012, *ApJS*, 203, 8
- Bodaghee, A., Tomsick, J. A., Rodriguez, J., & James, J. B. 2012, *ApJ*, 744, 108
- Boissier, S., Gil de Paz, A., Madore, B. F., et al. 2005, *ApJ*, 619, L83
- Bresolin, F., Ryan-Weber, E., Kennicutt, R. C., & Goddard, Q. 2009, *ApJ*, 695, 580
- Buccheri, R., Bennett, K., Bignami, G. F., et al. 1983, *A&A*, 128, 245
- Cappelluti, N., Brusa, M., Hasinger, G., et al. 2009, *A&A*, 497, 635
- Colbert, E. J. M., & Mushotzky, R. F. 1999, *ApJ*, 519, 89
- Condon, J. J., Cotton, W. D., Greisen, E. W., et al. 1998, *AJ*, 115, 1693
- Cowan, J. J., Roberts, D. A., & Branch, D. 1994, *ApJ*, 434, 128
- Craddock, R. G., Hasinger, G. R., & Schmitt, J. H. 1988, in *European Southern Observatory Conference and Workshop Proceedings*, eds. F. Murtagh, A. Heck, & P. Benvenuti, 28, 177
- Davidge, T. J. 2010, *ApJ*, 718, 1428
- de Vaucouleurs, G., de Vaucouleurs, A., Corwin, H. G., Jr., et al. 1992, *VizieR Online Data Catalog*: VII/137
- Di Stefano, R., & Kong, A. K. H. 2003, *ApJ*, 592, 884
- Di Stefano, R., Greiner, J., Murray, S., & Garcia, M. 2001, *ApJ*, 551, L37
- Done, C., Gierliński, M., & Kubota, A. 2007, *A&ARv*, 15, 1
- Dong, H., Calzetti, D., Regan, M., et al. 2008, *AJ*, 136, 479
- Dopita, M. A., Blair, W. P., Long, K. S., et al. 2010, *ApJ*, 710, 964
- Ehle, M., Pietsch, W., Beck, R., & Klein, U. 1998, *A&A*, 329, 39
- Fabbiano, G. 2006, *ARA&A*, 44, 323
- Fasano, G., & Franceschini, A. 1987, *MNRAS*, 225, 155
- Feng, H., & Soria, R. 2011, *New Astron. Rev.*, 55, 166
- Gilfanov, M. 2004, *MNRAS*, 349, 146
- Gladstone, J. C. 2010, *International Conference on Binaries: In celebration of Ron Webbink's 65th Birthday*, AIP Conf. Proc., 1314, 353
- Gottlieb, D. M., & Upson, II, W. L. 1969, *ApJ*, 157, 611
- Greiner, J. 2000, *New Astron.*, 5, 137
- Grimm, H.-J., Gilfanov, M., & Sunyaev, R. 2003, *MNRAS*, 339, 793
- Guainazzi, M. 2012, *XMM-Newton Calibration Technical Note*; XMM-SOC-CAL-TN-0018
- Güdel, M. 2002, *Roy. Soc. London Phil. Trans. Ser. A*, 360, 1935
- Harris, J., Calzetti, D., Gallagher, III, J. S., Conselice, C. J., & Smith, D. A. 2001, *AJ*, 122, 3046
- Hughes, J. P. 1994, *ApJ*, 427, L25
- Immler, S., Vogler, A., Ehle, M., & Pietsch, W. 1999, *A&A*, 352, 415
- Irwin, M., Maddox, S., & McMahon, R. 1994, *IEEE Spectrum*, 2, 14
- Johnson, H. L. 1966, *ARA&A*, 4, 193
- Jones, C. 1977, *ApJ*, 214, 856
- Jones, D. H., Saunders, W., Colless, M., et al. 2004, *MNRAS*, 355, 747
- Kahabka, P., & van den Heuvel, E. P. J. 1997, *ARA&A*, 35, 69
- King, A. R. 2009, *MNRAS*, 393, L41
- Koda, J., Yagi, M., Boissier, S., et al. 2012, *ApJ*, 749, 20
- Krautter, J., Zickgraf, F.-J., Appenzeller, I., et al. 1999, *A&A*, 350, 743
- Krumholz, M. R., & McKee, C. F. 2008, *Nature*, 451, 1082
- Kudritzki, R.-P., & Puls, J. 2000, *ARA&A*, 38, 613
- Long, K. S., Blair, W. P., Godfrey, L. E. H., et al. 2012, *ApJ*, 756, 18
- Maccacaro, T., Gioia, I. M., Wolter, A., Zamorani, G., & Stocke, J. T. 1988, *ApJ*, 326, 680
- Maddox, L. A., Cowan, J. J., Kilgard, R. E., et al. 2006, *AJ*, 132, 310
- Makishima, K., Maejima, Y., Mitsuda, K., et al. 1986, *ApJ*, 308, 635
- Meurer, G. R., Wong, O. I., Kim, J. H., et al. 2009, *ApJ*, 695, 765
- Miller, M. C., & Colbert, E. J. M. 2004, *Int. J. Mod. Phys. D*, 13, 1
- Mineo, S., Gilfanov, M., & Sunyaev, R. 2012, *MNRAS*, 419, 2095
- Misanovic, Z., Pietsch, W., Haberl, F., et al. 2006, *A&A*, 448, 1247
- Monet, D. G., Levine, S. E., Canzian, B., et al. 2003, *AJ*, 125, 984
- Ohashi, T., Makishima, K., Tsuru, T., et al. 1990, *ApJ*, 365, 180
- Okada, K., Mitsuda, K., & Dotani, T. 1997, *PASJ*, 49, 653
- Owen, R. A., & Warwick, R. S. 2009, *MNRAS*, 394, 1741
- Peacock, J. A. 1983, *MNRAS*, 202, 615
- Pietsch, W., Misanovic, Z., Haberl, F., et al. 2004, *A&A*, 426, 11
- Poutanen, J., Lipunova, G., Fabrika, S., Butkevich, A. G., & Abolmasov, P. 2007, *MNRAS*, 377, 1187
- Primini, F. A., Forman, W., & Jones, C. 1993, *ApJ*, 410, 615
- Puls, J., Vink, J. S., & Najarro, F. 2008, *A&ARv*, 16, 209
- Raymond, J. C., & Smith, B. W. 1977, *ApJS*, 35, 419
- Roberts, T. P., Warwick, R. S., Ward, M. J., Goad, M. R., & Jenkins, L. P. 2005, *MNRAS*, 357, 1363
- Roberts, T. P., Levan, A. J., & Goad, M. R. 2008, *MNRAS*, 387, 73
- Robrade, J., & Schmitt, J. H. M. M. 2010, *A&A*, 516, A38
- Rogstad, D. H., Lockhart, I. A., & Wright, M. C. H. 1974, *ApJ*, 193, 309
- Rosner, R., Golub, L., & Vaiana, G. S. 1985, *ARA&A*, 23, 413
- Rumstay, K. S., & Kaufman, M. 1983, *ApJ*, 274, 611
- Saha, A., Thim, F., Tammann, G. A., Reindl, B., & Sandage, A. 2006, *ApJS*, 165, 108
- Sako, M., Liedahl, D. A., Kahn, S. M., & Paerels, F. 1999, *ApJ*, 525, 921
- Schild, R. E. 1977, *AJ*, 82, 337
- Schröder, C., & Schmitt, J. H. M. M. 2007, *A&A*, 475, 677
- Schröder, C., Hubrig, S., & Schmitt, J. H. M. M. 2008, *A&A*, 484, 479
- Scoville, N., Aussel, H., Brusa, M., et al. 2007, *ApJS*, 172, 1
- Skrutskie, M. F., Cutri, R. M., Stiening, R., et al. 2006, *AJ*, 131, 1163
- Smith, R. K., Brickhouse, N. S., Liedahl, D. A., & Raymond, J. C. 2001, *ApJ*, 556, L91
- Soria, R., & Wu, K. 2002, *A&A*, 384, 99
- Soria, R., & Wu, K. 2003, *A&A*, 410, 53
- Soria, R., Long, K. S., Bianchi, L., et al. 2010, *The Astronomer's Telegram*, 3092, 1
- Soria, R., Kuntz, K. D., Winkler, P. F., et al. 2012, *ApJ*, 750, 152
- Stobart, A.-M., Roberts, T. P., & Wilms, J. 2006, *MNRAS*, 368, 397
- Tauris, T. M., & van den Heuvel, E. P. J. 2006, *Formation and evolution of compact stellar X-ray sources*, eds. W. H. G., Lewin, & M. van der Klis, 623
- Thilker, D. A., Bianchi, L., Boissier, S., et al. 2005, *ApJ*, 619, L79
- Thim, F., Tammann, G. A., Saha, A., et al. 2003, *ApJ*, 590, 256
- Tilanus, R. P. J., & Allen, R. J. 1993, *A&A*, 274, 707
- Treves, A., Maraschi, L., & Abramowicz, M. 1988, *PASP*, 100, 427
- Trinchieri, G., Fabbiano, G., & Palumbo, G. G. C. 1985, *ApJ*, 290, 96
- Tully, R. B. 1988, *Nearby galaxies catalog*
- Turner, T. J., Weaver, K. A., Mushotzky, R. F., Holt, S. S., & Madejski, G. M. 1991, *ApJ*, 381, 85
- Vaiana, G. S., Cassinelli, J. P., Fabbiano, G., et al. 1981, *ApJ*, 245, 163
- van den Heuvel, E. P. J., Bhattacharya, D., Nomoto, K., & Rappaport, S. A. 1992, *A&A*, 262, 97
- van Paradijs, J. 1998, in *The Many Faces of Neutron Stars*, eds. R. Buccheri, J. van Paradijs, & A. Alpar, NATO ASIC Proc., 515, 279
- Vaughan, B. A., van der Klis, M., Wood, K. S., et al. 1994, *ApJ*, 435, 362
- Vignali, C., Comastri, A., Capri, M., et al. 1999, *ApJ*, 516, 582
- Walter, R., & Fink, H. H. 1993, *A&A*, 274, 105
- White, N. E., & Carpenter, G. F. 1978, *MNRAS*, 183, 11
- White, N. E., & Marshall, F. E. 1984, *ApJ*, 281, 354
- White, N. E., Nagase, F., & Parmar, A. N. 1995, in *X-ray Binaries*, 1
- Wofford, A., Leitherer, C., & Chandar, R. 2011, *ApJ*, 727, 100

Appendix A: Classification and identification of the *XMM-Newton* sources

A.1. Foreground stars

Sources Nos. 21, 143, 182, and 174. Using the criteria in Sect. 5.1, we classified sources Nos. 21, 143, 182, and 174 as foreground stars according to their optical and infrared properties (Figs. 4, 6), and their optical-to-X-ray ratios as a function of the hardness ratios (Fig. 5). Although the hardness ratio criterion $HR_3 \lesssim -0.4$ of source No. 174 is not fulfilled, we classified this source as a foreground star because of the large uncertainty of the hardness ratio (see Fig. 5).

Source No. 24 has optical and infrared counterparts and $\log_{10}(f_x/f_{\text{opt}}) < -1$, but violates the hardness ratio HR_2 criterion (see Fig. 5). The optical counterpart is bright ($m_{B,\text{No. 24}} = 14.1$), and the $B-R$ and $J-K$ colours are consistent with those of foreground stars (Figs. 4 and 6), thus this source most likely belongs to the Milky Way. It has been detected in observations 1 and 2 in all three EPIC cameras. In all cases, source No. 24 shows hard HR_2 (Fig. 5, left panel), inconsistent with the expected X-ray spectra of foreground stars. The properties of the optical companion and the hard X-ray spectra may indicate a cataclysmic-variable nature for this source. This class of sources can show short- and long-term time variability, therefore we produced the X-ray lightcurve in the energy range 0.5–4.5 keV to give more evidence for this identification. However, the resulting X-ray lightcurve (with a bin-time of 2000 s) shows neither short- nor long-term variability.

A.2. Sources that are not foreground stars

Sources Nos. 12, 137, 164, and 189 coincide with ROSAT sources H2, H31, H34 and H36. They were classified by Immler et al. (1999) as foreground stars based on positional coincidences with optical sources of the *APM Northern Sky Catalogue* (Irwin et al. 1994). We found possible optical counterparts in the USNO-B1 catalogue for source No. 164 (USNO-B1 0601 – 0299090) and source No. 12 (USNO-B1 0602 – 0301227). However, their X-ray-to-optical flux ratios (Eq. (2)) are $\log(f_x/f_{\text{opt}}) \approx 0.10$ and 0.11 respectively (f_{opt} of both sources was calculated using visual magnitude), hence the foreground star classification for these sources is ruled out. The refined positions of sources Nos. 137 and 189 obtained with *XMM-Newton*, allowed us to exclude their association with the optical counterparts proposed by Immler et al. (1999). Source No. 189 can be associated with a new optical counterpart, USNO-B1 0600 – 0300832, which is ~ 3 orders of magnitude fainter than the previous one (USNO-B1 0600 – 0300831). However, the new X-ray-to-optical flux ratio is $\log(f_x/f_{\text{opt}}) \approx 0.68$ (f_{opt} was calculated using visual magnitude), too high for a foreground star (see Sect. A.3). Hardness ratios of sources Nos. 164 and 137 are consistent with a powerlaw or disk-blackbody spectrum. Therefore, the spectra of these sources are too hard to be classified as foreground stars.

A.3. Background objects

We found radio counterparts of the sources Nos. 20, 37, and 189 and classified them as AGN candidates for the first time.

Source No. 20 is located outside the D_{25} ellipse ($D_{25} = 11.5'$; Tully 1988) at $\sim 0.41^\circ$ from the centre of the galaxy. It coincides with the radio source NVSS J133618–301459. We detected this source with *XMM-Newton* in observations 2 and 3 in the outer disc of M 83. Source No. 20 shows a significant long-term variability (Table 3), and the hardness ratios are roughly consistent with a spectrum described by an APEC model with a temperature of $kT_{\text{apec}} \sim 0.5$ keV ($HR_2 = -0.2 \pm 0.1$; $HR_3 = -0.81 \pm 0.11$). Therefore, source No. 20 can be classified as an AGN candidate (with a soft spectral component) or an SNR candidate. The distance of this source from the nuclear region of M 83 of ~ 32 kpc rather indicates that source No. 20 does not belong to the galaxy, therefore it is more likely an AGN than an SNR candidate.

Sources Nos. 37 and 189 coincide with the radio sources NVSS J133630–301651 and NVSS J133805–295748, respectively. Source No. 189 was previously classified as a foreground star by Immler et al. (1999) (see Sect. A.2). We detected these sources with *XMM-Newton* in observation 3. Their hardness ratios are consistent with a spectrum described with a powerlaw or disc-blackbody model (No. 37: $HR_2 = 0.62 \pm 0.12$; $HR_3 = -0.37 \pm 0.13$; No. 189: $HR_2 = 0.07 \pm 0.10$; $HR_3 = -0.25 \pm 0.12$). Therefore, they can be classified as AGN candidates.

A.4. X-ray binaries

Source No. 81 coincides with the *Chandra* source [SW03] 33, classified as an accreting X-ray pulsar, with a hard spectrum ($\Gamma \approx 1.7$) and a spin period of 174.9 s.

We observed source No. 81 in all *XMM-Newton* observations. The hardness ratios are consistent with an absorbed powerlaw spectrum, and this source shows a significant long-term X-ray variability ($V_f = 2.5$, $S = 3.0$, Table 3). We applied a Fourier transform periodicity search and a Z_n^2 analysis (Sect. 4.1), which did not reveal any significant periodicity. We calculated the upper-limit on the pulsed fraction (defined as the semi-amplitude of the sinusoidal modulation divided by the mean count rate) using the procedure described by Vaughan et al. (1994). The upper limit on the pulsed fraction obtained from the combined PN and MOS events of observation 1 is 16% at the 99% confidence level. This upper limit is marginally compatible with the pulsed fraction of $(50 \pm 15)\%$ of source [SW03] 33.

Source No. 120 corresponds to the X-ray source [SW03] 113. Using the spectral properties and the 201.5 s periodicity detected with *Chandra*, SW03 classified source [SW03] 113 as an XRB in a soft state.

We observed source No. 120 with *XMM-Newton* in observations 1 and 3. The hardness ratios of this source are consistent with an absorbed powerlaw spectrum with $N_H \sim 5 \times 10^{21} \text{ cm}^{-2}$ and $\Gamma \sim 1.5$. Similarly to source No. 81, a Fourier transform periodicity search and a Z_n^2 analysis did not reveal any significant periodicity. At the 99% confidence level, the upper limit on the pulsed-fraction of source No. 120 derived from the MOS events is 49%. This upper limit is compatible with the $(50 \pm 19)\%$ pulsed fraction of [SW03] 113.

A.5. Supernova remnant candidates

Source No. 79. The position of this source corresponds to the position of the ROSAT source H15 (Immler et al. 1999) and the *Chandra* source [SW03] 27. The *Chandra* spectrum shows emission lines, suggesting the possibility of emission from optically thin thermal plasma, and has been fitted by SW03 with

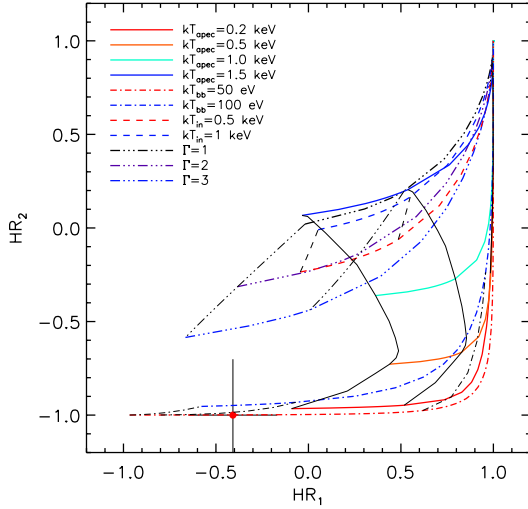


Fig. A.1. Hardness-ratio diagram of source No. 91 observed with *XMM-Newton*. Thick lines are different spectral models as function of the N_H , thin lines are different column densities N_H (from left to right: 10^{20} , 10^{21} , 10^{22} cm $^{-2}$) as a function of the spectral parameters.

an absorbed powerlaw with $\Gamma \sim 1.4$ and $N_H \sim 7 \times 10^{20}$ cm $^{-2}$. SW03 classified this source as a young SNR candidate. Another possible explanation for the hard powerlaw spectrum with superposition of emission lines of [SW03] 27 is that the source is an XRB surrounded by a photoionised nebula (SW03). However, XRBs showing these spectral properties usually have a higher absorbing column density than that of [SW03] 27 (see e.g. Sako et al. 1999).

The *XMM-Newton* hardness ratios of source No. 79 below 2 keV are consistent with an APEC model with temperature $kT_{\text{apec}} \gtrsim 1.5$ keV, while at higher energies the hardness ratios are consistent with a powerlaw with photon index ~ 2 . The spectral shape of source No. 79 derived from *XMM-Newton* hardness-ratio diagrams agrees with the X-ray spectrum of [SW03] 27 presented by SW03 (see Fig. 6 in SW03) and can be interpreted as an SNR exhibiting both a thin-thermal emission (below ~ 2 keV) and an additional hard component, which dominates at energies above ~ 2 keV. Also, source No. 79 does not show any significant long-term variability (see Table 3).

A.6. Super-soft source candidates

Source No. 91 coincides with *Einstein* source 3 (Trinchieri et al. 1985) and *Chandra* source [SW03] 55 classified by Di Stefano & Kong (2003) as an SSS candidate (source M 83-50 in Di Stefano & Kong 2003). Di Stefano & Kong (2003) fitted the X-ray spectrum of M 83-50 with an absorbed blackbody with a temperature of $kT_{\text{bb}} = 66^{+13}_{-24}$ eV, a column density of $N_H = 2.4^{+7.4}_{-2.4} \times 10^{20}$ cm $^{-2}$, and a luminosity of $L_x = 2.8 \times 10^{37}$ erg s $^{-1}$ (0.3–7 keV, $d = 4.5$ Mpc).

We detected source No. 91 in observation 1, where the hardness ratios are consistent with a blackbody spectrum (with column density in the range $\approx 10^{20}$ – 10^{21} cm $^{-2}$) and marginally compatible with an APEC spectrum with temperature in the range ≈ 0.2 – 0.5 keV (Fig. A.1). Source No. 91 has a 0.2–4.5 keV luminosity of $L_x = (2.2 \pm 0.2) \times 10^{37}$ erg s $^{-1}$ and does not show any significant variability compared to the *Chandra* observation.

A.7. Ultra-luminous X-ray sources

Two ULXs have been discovered in M 83: H2 (Trinchieri et al. 1985), and a transient ULX discovered with *Chandra* on

23 December 2010 with a luminosity of $L_x \sim 4 \times 10^{39}$ erg s $^{-1}$ (0.3–10 keV) by Soria et al. (2010), and classified as an accretion-powered black hole with mass $M_{\text{BH}} \approx 40$ – $100 M_\odot$ (Soria et al. 2012). This ULX has not been detected in the *XMM-Newton* data. Soria et al. (2012) measured an upper limit to the X-ray luminosity of $\sim 10^{37}$ erg s $^{-1}$ (0.3–10 keV) from the three *XMM-Newton* observations.

Source No. 133. We observed the ULX as source No. 133 in all *XMM-Newton* observations. Ehle et al. (1998) and Immler et al. (1999) found a faint extended optical source within the error circle of the ROSAT source position. Roberts et al. (2008) used HST images in three Advanced Camera for Survey (ACS) filters to find the counterparts to six ULXs in different galaxies. For the ULX in M 83, they compared the optical position with the X-ray position from a *Chandra* High Resolution Camera for Imaging (HRC-I) observation. They detected a counterpart to the ULX with magnitudes $B = 25.66 \pm 0.13$, $V = 25.36 \pm 0.17$. They also noticed that the ULX is located at $\sim 5''$ from the centre of a background galaxy, and although the latter is outside the error circle, Roberts et al. (2008) did not completely rule out a possible association between the ULX and the background galaxy.

Stobbart et al. (2006) reported the *XMM-Newton* spectral analysis of source No. 133 during observation 1. They found that the X-ray spectrum is well fitted with a cool disc-blackbody ($kT_{\text{in}} \sim 0.2$ keV) plus a powerlaw ($\Gamma \sim 2.5$), or with a cool blackbody ($kT_{\text{bb}} \sim 0.2$ keV) plus a warm disc-blackbody ($kT_{\text{in}} \sim 1.1$ keV). The first spectral model is the standard IMBH model, where the low disc temperature is due to a black hole with mass of $\sim 1000 M_\odot$, while the origin of the powerlaw component is still not clear (see Roberts et al. 2005). Instead, the spectral parameters obtained with the second spectral model suggest that No. 133 is a stellar-mass black hole accreting close to the Eddington limit. In this model, the cool blackbody component represents the optically thick wind from the stellar-mass black-hole accreting at or above the Eddington limit, while the high temperature of the disc follows the standard trend $L_x \propto T^4$ shown by the Galactic stellar-mass black-hole binaries.

We analysed all *XMM-Newton* observations of the ULX No. 133 and fitted the PN, MOS1 and MOS2 spectra simultaneously with a model assuming an IMBH (PHABS*[DISKBB + POWERLAW] in XSPEC), and a model assuming a stellar-mass BH (PHABS*[BBODY + DISKBB]). We used two absorption components: the Galactic absorption column density ($N_H = 3.69 \times 10^{20}$ cm $^{-2}$) and the absorption within M 83 plus the intrinsic column density of the ULX. In all fits we obtained a good fit with both spectral models with the resulting spectral parameters in agreement with those obtained by Stobbart et al. (2006) from observation 1. However, the spectral parameters in observation 3 are only poorly constrained due to the poor statistics (only MOS1 and MOS2 data were available for this observation). Therefore, we fitted the spectrum of observation 3 with a single component model and found that an absorbed powerlaw can adequately fit the data (Fig. A.2, Table A.1).

A.8. Hard sources

A.8.1. New classifications

Source No. 16 coincides with the ROSAT source H3 discovered by Immler et al. (1999). This source is located outside the optical disc of M 83, and its position overlaps with the outer disc of M 83 observed by GALEX (e.g. Thilker et al. 2005).

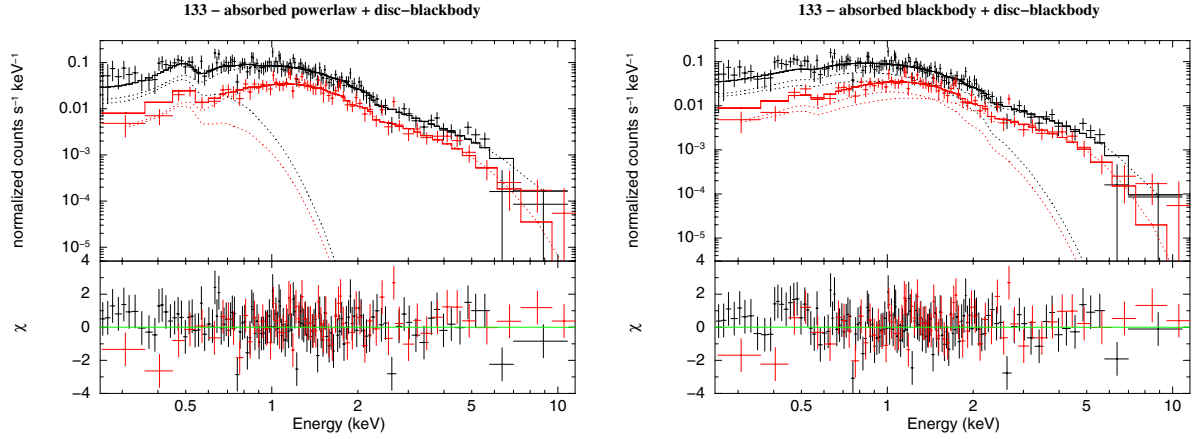


Fig. A.2. EPIC counts spectra, together with residuals in units of standard deviations for source No. 133 detected in the observation 2. *Left panel* shows the fit with an absorbed cool disc-blackbody plus hard powerlaw, while the *right panel* shows the fit with an absorbed cool blackbody plus a warm disc-blackbody (see Table A.1).

Table A.1. Best-fitting parameters of the X-ray spectra of source No. 133 (errors at 90% confidence level).

	Obs. 2		Obs. 3
Model	POWERLAW + DISKBB	BBODY + DISKBB	POWERLAW
N_H (10^{22} cm $^{-2}$)	$0.30^{+0.12}_{-0.09}$	≤ 0.03	0.12 ± 0.05
Γ or kT_{bb} (keV)	$2.64^{+0.19}_{-0.18}$	$0.30^{+0.02}_{-0.04}$	$2.6^{+0.3}_{-0.2}$
Norm.	$4.4^{+1.0}_{-0.4} \times 10^{-4}$	$3.6^{+0.8}_{-0.9} \times 10^{-6}$	$1.4^{+0.3}_{-0.3} \times 10^{-4}$
kT_{in} (keV)	$0.09^{+0.02}_{-0.03}$	$1.4^{+0.3}_{-0.2}$	
Norm.	$4.8^{+47.4}_{-4.4} \times 10^3$	$7.8^{+9.7}_{-3.1} \times 10^{-3}$	
χ^2_v (d.o.f.)	0.946 (184)	0.994 (184)	0.918 (62)
F_x (0.2–12 keV, erg cm $^{-2}$ s $^{-1}$)	$8.9^{+57.5}_{-3.7} \times 10^{-13}$	$8.5^{+24.5}_{-5.2} \times 10^{-13}$	$3.7^{+2.2}_{-1.4} \times 10^{-13}$
L_x ($d = 4.5$ Mpc, erg s $^{-1}$)	$1.3^{+20.4}_{-0.6} \times 10^{40}$	$2.2^{+6.3}_{-1.3} \times 10^{39}$	$2.2^{+0.9}_{-0.5} \times 10^{39}$

Table A.2. Best-fitting parameters of sources No. 16, 61, 103, 126, 153.

Source	Parameters						Analysed data	
	N_H (10^{21} cm $^{-2}$)	Γ	Norm.	χ^2_v (d.o.f.)	F_x (erg cm $^{-2}$ s $^{-1}$)	L_x (erg s $^{-1}$)	Obs.	Instrument
16	$0.8^{+0.4}_{-0.3}$	$2.6^{+0.3}_{-0.3}$	$4.1^{+0.9}_{-0.7} \times 10^{-5}$	0.928 (38)	$1.4^{+0.8}_{-0.5} \times 10^{-13}$	$6.3^{+2.7}_{-1.3} \times 10^{38}$	1	PN, MOS1, MOS2
61	$2.01^{+0.75}_{-0.65}$	$2.4^{+0.3}_{-0.3}$	$2.9^{+0.9}_{-0.6} \times 10^{-5}$	1.04 (36)	$8.0^{+6.8}_{-3.7} \times 10^{-14}$	$4.3^{+1.4}_{-0.6} \times 10^{38}$	1	PN, MOS1, MOS2
103	$0.7^{+1.0}_{-0.7}$	$1.8^{+0.4}_{-0.4}$	$3.7^{+1.8}_{-1.2} \times 10^{-5}$	0.876 (19)	$2.2^{+3.3}_{-1.3} \times 10^{-13}$	$6.6^{+6.7}_{-2.7} \times 10^{38}$	1	PN, MOS2
126	$0.01^{+0.56}_{-0.01}$	$1.8^{+0.4}_{-0.2}$	$8.8^{+2.7}_{-1.2} \times 10^{-6}$	0.743 (17)	$6.3^{+3.1}_{-2.9} \times 10^{-14}$	$1.5^{+0.8}_{-0.4} \times 10^{38}$	2	PN, MOS1, MOS2
153	$0 < N_H \leq 1.5$	$1.4^{+0.7}_{-0.3}$	$7.6^{+5.8}_{-1.6} \times 10^{-6}$	1.027 (15)	$8.8^{+13.7}_{-6.2} \times 10^{-14}$	$2.1^{+3.3}_{-1.2} \times 10^{38}$	1	PN, MOS1, MOS2

Notes. We fitted the spectra with an absorbed powerlaw. Γ is the powerlaw photon-index, F_x is the absorbed flux in the energy range 0.2–12 keV, L_x is the X-ray luminosity in the same energy range of F_x (errors at 90% confidence level).

We detected source No. 16 in all *XMM-Newton* observations, but only in observation 1 was it bright enough to allow spectral analysis. The spectrum can be well fitted with an absorbed powerlaw with $\Gamma = 2.6^{+0.3}_{-0.3}$, compatible with that of an XRB or an AGN (see Table A.2). Source No. 16 shows a significant long-term variability ($S = 9.5$) with a variability factor of $V_f = 10.6 \pm 0.3$ (Table 3). It also shows a significant variability within observation 1, with a variability factor of $V_f = 6.6 \pm 4.5$ and significance $S = 4.0$.

Source No. 61 is in the field of view of *XMM-Newton* during observation 1, where it shows an X-ray luminosity of $L_x \approx 4 \times 10^{38}$ erg s $^{-1}$ (see Table A.2). It has not been previously detected

in X-ray, optical, radio, infrared, or UV. The X-ray spectrum is well fitted with an absorbed powerlaw with $\Gamma = 2.4^{+0.3}_{-0.3}$ or a disc-blackbody model with temperature $kT_{in} = 0.82^{+0.13}_{-0.11}$ keV (Table A.2). Source No. 61 shows a significant long-term variability ($S = 8.6$) with a variability factor of $V_f = 4.3 \pm 0.1$ (Table 3).

Source No. 103 is located at a distance of $\sim 6''$ from a radio source (6 in Cowan et al. 1994, 36 in Maddox et al. 2006), and at $1.6''$ from the *Chandra* source [SW03]84, which shows hardness ratios compatible with a powerlaw or a disc-blackbody spectrum.

Table A.3. Best-fitting parameters of sources Nos. 97, 106, 107, 108, 114, and 129.

Source	Parameters						Analysed data	
	N_{H} (10^{21} cm^{-2})	Γ	Norm.	χ^2_{ν} (d.o.f.)	F_{x} ($\text{erg cm}^{-2} \text{ s}^{-1}$)	L_{x} (erg s^{-1})	Obs.	Instrument
97	$4.4^{+1.1}_{-0.9}$	$2.4^{+0.3}_{-0.3}$	$7.4^{+2.3}_{-1.7} \times 10^{-5}$	1.03 (45)	$1.7^{+1.5}_{-0.8} \times 10^{-13}$	$1.1^{+0.4}_{-0.2} \times 10^{39}$	1	PN, MOS2
106	$0.3^{+0.5}_{-0.3}$	$1.8^{+0.4}_{-0.3}$	$8.3^{+2.5}_{-1.9} \times 10^{-6}$	1.38 (27)	$5.4^{+5.0}_{-2.7} \times 10^{-14}$	$1.5^{+1.0}_{-0.5} \times 10^{38}$	1	PN, MOS1, MOS2
107	$3.3^{+1.0}_{-0.8}$	$2.8^{+0.4}_{-0.3}$	$3.9^{+1.4}_{-1.0} \times 10^{-5}$	0.821 (43)	$6.5^{+6.5}_{-3.3} \times 10^{-14}$	$6.6^{+5.1}_{-2.3} \times 10^{38}$	1	PN, MOS1, MOS2
108	$3.3^{+0.7}_{-0.6}$	$2.7^{+0.3}_{-0.2}$	$8.0^{+1.9}_{-1.5} \times 10^{-5}$	0.91 (68)	$1.5^{+0.9}_{-0.6} \times 10^{-13}$	$1.3^{+0.5}_{-0.3} \times 10^{39}$	1	PN, MOS1
114	$4.5^{+3.8}_{-3.1}$	$1.7^{+0.4}_{-0.4}$	$1.8^{+1.3}_{-0.7} \times 10^{-5}$	0.952 (20)	$9.6^{+24.0}_{-6.9} \times 10^{-14}$	$3.5^{+5.68}_{-1.8} \times 10^{38}$	1	PN, MOS1, MOS2
129	$5.4^{+4.3}_{-3.0}$	$2.0^{+0.6}_{-0.5}$	$2.0^{+1.9}_{-0.9} \times 10^{-5}$	0.867 (18)	$6.7^{+20.9}_{-5.1} \times 10^{-14}$	$3.1^{+5.4}_{-1.4} \times 10^{38}$	1	PN, MOS1

Notes. We fitted the spectra with an absorbed powerlaw. Γ is the powerlaw photon-index, F_{x} is the absorbed flux in the energy range 0.2–12 keV, L_{x} is the X-ray luminosity in the same energy range of F_{x} (errors at 90% confidence level).

We detected source No. 103 only in the *XMM-Newton* observation 2, with a flux of $(2.23^{+3.26}_{-1.34}) \times 10^{-13} \text{ erg cm}^{-2} \text{ s}^{-1}$ (0.2–12 keV). The X-ray spectrum is well fitted with an absorbed powerlaw with $\Gamma = 1.8^{+0.4}_{-0.4}$ (Table A.2). We did not detect source No. 103 in observations 1 and 3, thus we calculated the flux upper-limits and we found a significant ($S = 7.2$) long-term variability, with a variability factor of $V_{\mathrm{f}} = 12.78 \pm 0.12$ (Table 3, Fig. 2).

Source No. 126 coincides with X-ray source 30 (Ehle et al. 1998) discovered with ROSAT. Source No. 126 also cross-correlates with the optical counterpart USNO-B1 0599 – 0300335, but the ratio $\log_{10}(F_{\mathrm{x}}/F_{\mathrm{opt}})$ does not match the criteria previously specified to classify foreground stars. Source No. 126 is located outside the optical disc of M 83, and its position overlaps with an extended arm of the galaxy.

We observed source No. 126 in all *XMM-Newton* observations. The X-ray spectra extracted from each observation can be well fitted with an absorbed powerlaw with $\Gamma \approx 1.8$ and the flux is consistent with that measured by Ehle et al. (1998) (Table A.2).

Source No. 153 is detected in all *XMM-Newton* observations, and has not been previously detected in X-rays, optical, radio, infrared, or UV bands. It is located in the extended arms observed by GALEX, $\approx 10'$ away from the nuclear region of M 83.

The spectra extracted from each observation can be well fitted with an absorbed powerlaw with $\Gamma \approx 1.5$, suggesting an XRB nature for this source (see Table A.2).

A.8.2. Identifications

Source No. 60 correlates with the *Chandra* source [SW03] 5. SW03 suggested that this source is an XRB candidate.

We observed source No. 60 in all *XMM-Newton* observations. The source shows a significant long-term variability ($V_{\mathrm{f}} = 2.4$, $S = 3.8$, Table 3) with respect to the *Chandra* observation. X-ray colours of No. 60 are consistent with a powerlaw or disc-blackbody spectrum, in agreement with the spectral analysis of SW03.

Source No. 80 correlates with the *Chandra* source [SW03] 31. From the spectral properties, SW03 suggested that [SW03] 31 is an XRB candidate.

We observed source No. 80 with *XMM-Newton* in observation 1. The hardness ratios are consistent with a powerlaw or disc-blackbody spectrum with column density of $\sim 10^{21} \text{ cm}^{-2}$.

Source No. 92 coincides with the *Chandra* source [SW03] 60. SW03 suggested that No. 92 is a XRB candidate because of its hard spectrum ($\Gamma \sim 1.6$).

We observed source No. 92 with *XMM-Newton* in observation 1. The hardness ratios are consistent with a spectrum described by an absorbed powerlaw model with $\Gamma \sim 2$. Source No. 92 also shows a high long-term variability by a factor of $V_{\mathrm{f}} = 2.7$, with a variability significance of $S = 4.3$ (see Table 3).

Source No. 97 coincides with the *Chandra* source [SW03] 72 and with a ROSAT source (source 7 in Ehle et al. 1998 and source H20 in Immler et al. 1999).

We observed source No. 97 in all *XMM-Newton* observations. The spectra extracted from each observation can be well fitted with an absorbed powerlaw or a disc-blackbody model (Table A.3), with spectral parameters in agreement with the spectral analysis of SW03. Source No. 97 shows a significant long-term variability between *XMM-Newton* and *Chandra* observations ($V_{\mathrm{f}} = 2.8 \pm 0.1$, $S = 6.6$; Table 3). Within observation 1 we found a variability of $V_{\mathrm{f}} = 6.4 \pm 2.7$ with a significance of $S = 4.8$.

Source No. 99 coincides with the *Chandra* source [SW03] 73, and it is associated with the radio source MCK 34 (Maddox et al. 2006), located in a HII region (RK 137, Rumstay & Kaufman 1983). From a spectral study, SW03 proposed that [SW03] 73 is more likely an XRB than a young SNR.

We observed source No. 99 with *XMM-Newton* in observations 2 and 3. The source shows a significant variability ($S = 5.0$), with a variability factor of $V_{\mathrm{f}} = 15.3$ (Table 3), and the hardness ratios are consistent with an absorbed powerlaw or disk-blackbody spectrum.

Source No. 106 corresponds to the X-ray source H25 observed by Immler et al. (1999) in a ROSAT observation and the *Chandra* source [SW03] 85.

We observed source No. 106 in all the observations. During observation 1 the source was bright enough to allow spectral analysis. The spectrum can be well fitted with an absorbed powerlaw (see Table A.3), with spectral parameters in agreement with those previously obtained by SW03.

Source No. 107 was detected by [Ehle et al. \(1998\)](#) (source 9) and [Immler et al. \(1999\)](#) (source H26) in ROSAT (PSPC and HRI) observations. [Immler et al. \(1999\)](#) found that H26 coincides with a compact radio source (source 8 in [Cowan et al. 1994](#)), and with a giant HII region ([Rumstay & Kaufman 1983](#)). Hence, they classified this source as an SNR candidate. Moreover, also the observation of $H\alpha$ and $H\beta$ emission anti-coincident with HI emission ([Tilanus & Allen 1993](#)) supports the SNR hypothesis. Source No. 107 was also observed in 2000 April 29 by *Chandra* (source [SW03] 86). From a spectral analysis, SW03 proposed that No. 110 is more likely an XRB (BH candidate) than an SNR.

We detected source No. 107 in all *XMM-Newton* observations with a luminosity of $\sim 7 \times 10^{38} \text{ erg s}^{-1}$. In observations 1 and 3 the source was bright enough to allow spectral analysis. The spectra can be well fitted with an absorbed powerlaw or a disc-blackbody (see Table A.3). The obtained spectral parameters are consistent with those previously found by SW03 with *Chandra*. Source No. 107 shows a significant long-term variability between *XMM-Newton* observations ($V_f = 1.97 \pm 0.12$, $S = 5.1$).

Source No. 108 was first detected in X-rays by [Trinchieri et al. \(1985\)](#) (source 4) with the *Einstein* satellite and by [Ehle et al. \(1998\)](#) (source 8) and [Immler et al. \(1999\)](#) (source H27) with ROSAT. It also coincides with the *Chandra* source [SW03] 88.

We observed source No. 108 in all *XMM-Newton* observations. During observation 1 source No. 108 was in the centre of the field of view, providing enough statistic to allow spectral analysis. We extracted the PN and MOS1 spectra (the position of source No. 108 was in a gap of MOS2) and we found that an absorbed powerlaw or an absorbed disc-blackbody provide acceptable fits (Table A.3), with spectral parameters consistent with those obtained by SW03. Source No. 108 shows a significant long-term X-ray variability ($V_f = 1.4 \pm 0.1$, $S = 3.3$, Table 3), and during observation 1 we found a variability of $V_f = 4.2 \pm 1.5$, with a significance of $S = 4.4$.

Source No. 114 coincides with the *Chandra* source [SW03] 104.

We observed source No. 114 in all *XMM-Newton* observations. During observation 1 source No. 114 was in the centre of the field of view, providing enough statistics to allow a spectral analysis. The spectrum is well fitted with an absorbed powerlaw with spectral parameters consistent with those found by SW03 with *Chandra* (see Table A.3). Source No. 114 also shows a significant long-term variability ($V_f = 2.4 \pm 0.2$, $S = 4.1$).

Source No. 116 coincides with [SW03] 105. [Di Stefano & Kong \(2003\)](#) observed [SW03] 105 with *Chandra* (source M 83-88 in [Di Stefano & Kong 2003](#)) and classified it as an SSS candidate. [Blair & Long \(2004\)](#) compared the list of *Chandra*

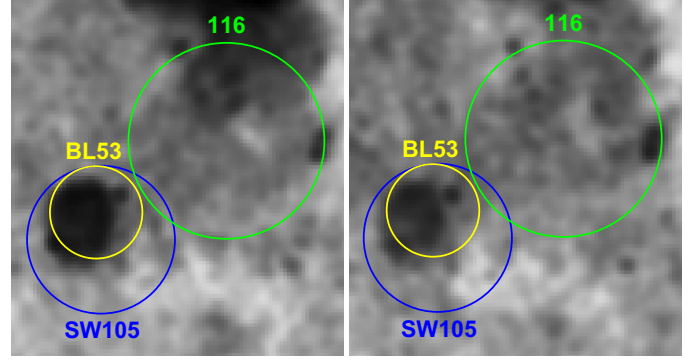


Fig. A.3. Emission line HST/WFC3 images of the region surrounding source No. 116. *Left panel:* WFC3 image with the narrowband filter F657N, corresponding to $H\alpha$ line emission. *Right panel:* WFC3 image with the narrowband filter F673N, corresponding to SII line emission. The radii of the circles of *Chandra* (SW105) and *XMM-Newton* (116) sources give the 3σ accuracy of the position of the sources. The circle labelled BL53 gives the position of the optical SNR candidate.

sources of SW03 with a list of optical SNR candidates and associated [SW03] 105 with the optical SNR candidate BL53.

We observed source No. 116 with *XMM-Newton* in observation 1, where it shows a significant X-ray variability ($V_f = 20.8$, $S = 6.2$, Table 3) compared to the *Chandra* observation, and the X-ray hardness ratios are consistent with a hard spectrum. These properties indicate that source No. 116 is most likely an XRB. We overlaid the 3σ error circles of source No. 116, [SW03] 105, and BL53 on the emission line images $H\alpha$ and SII obtained from the public *Wide Field Camera 3* (WFC3) observation of 2009-08-20 (Fig. A.3). $H\alpha$ and SII images are used in extragalactic searches of SNRs because their optical spectra show high [SII]: $H\alpha$ ratios compared to the spectra of normal HII regions (see e.g. [Blair & Long 2004](#)). Fig. A.3 shows that the shell of the optical SNR is located only in the error circles of BL53 and [SW03] 105, indicating that source No. 116 and [SW03] 105 cannot be the same source.

Therefore, source No. 116 is more likely a transient source not associated with BL53.

Source No. 129 coincides with the *Chandra* source [SW03] 121 and with a ROSAT source (source 12 in the catalogue of [Ehle et al. 1998](#), source H29 in the catalogue of [Immler et al. 1999](#)).

We observed source No. 129 during observation 1, where it was in the *XMM-Newton* field of view. The spectrum is well fitted with an absorbed powerlaw with spectral parameters consistent with those found by SW03 with *Chandra* (see Table A.3). We did not detect source No. 129 in observations 2 and 3, thus we calculated the flux upper limits and we found a significant ($S \gtrsim 6.4$) long-term variability with a variability factor of $V_f = 3.94 \pm 0.11$ (Table 3).